

## Article

# Energy Dissipation Analysis of Contact/Impact of Deformable Bodies Using Numerical Modelling

Ondřej Holíš <sup>1</sup>, Tomáš Dvořák <sup>1</sup>, Matej Koiš <sup>1</sup>, Ivan Němec <sup>2</sup>, Miroslav Trcala <sup>3</sup> and Jiří Vala <sup>3,\*</sup>

<sup>1</sup> Institute of Structural Mechanics, Faculty of Civil Engineering, Brno University of Technology, 602 00 Brno, Czech Republic; ondrej.holis@vut.cz (O.H.); tomas.dvorak11@vut.cz (T.D.); 226837@vut.cz (M.K.)

<sup>2</sup> FEM Consulting Ltd., 602 00 Brno, Czech Republic; nemec@fem.cz

<sup>3</sup> Institute of Mathematics and Descriptive Geometry, Faculty of Civil Engineering, Brno University of Technology, 602 00 Brno, Czech Republic; miroslav.trcala@vut.cz

\* Correspondence: jiri.vala@vut.cz

## Abstract

The numerical analysis of dissipative energy in dynamic problems involving impact and contact phenomena relies on the physical principles of classical thermodynamics and on the constitutive equations of the material, supplemented by some additional considerations of potential contact interfaces. From the mathematical perspective, we come to a weak form of partial differential equation(s) of evolution with initial, boundary, and interface conditions, whose numerical analysis is required using the method of discretisation in time and typically the finite element technique. Dissipative energy is an important metric for quantifying the portion of mechanical work that is permanently converted to plastic work and thermal energy, among other applications. Crucially, the localised accumulation of this energy, often expressed as the plastic work density, is the primary physical parameter driving microstructural changes, damage initiation, and crack propagation under intense loading. This paper demonstrates how the dissipative energy resulting from material nonlinearities can be evaluated in dynamic problems involving the impact of one body on another and provides a quantitative comparison of numerically calculated dissipated energy using three types of nonlinear constitutive material models, namely the plastic material model with Rankine–Hill criterion, the Mazars damage model, and the Kelvin–Voigt viscoelastic model.

**Keywords:** building materials; dynamic contact/impact of deformable bodies; dissipative energy; computational modelling

**PACS:** 46.55.+d; 46.35.+z; 02.70.Dh; 02.70.Bf; 02.30.Jr



Academic Editor: Antonio Formisano

Received: 22 December 2025

Revised: 20 January 2026

Accepted: 26 January 2026

Published: 31 January 2026

**Copyright:** © 2026 by the authors.

Licensee MDPI, Basel, Switzerland.

This article is an open access article

distributed under the terms and

conditions of the [Creative Commons](https://creativecommons.org/licenses/by/4.0/)

[Attribution \(CC BY\)](https://creativecommons.org/licenses/by/4.0/) license.

## 1. Introduction

Numerical modelling and the simulation of strain and stress development in deformable bodies under various types of mechanical, thermal, etc., loads at the macroscopic level for engineering applications relies on the principles of classical thermodynamics, summarised in [1,2], namely the conservation of mass, (linear and angular) momentum, and energy. This formulation must be supplied by appropriate constitutive relations, motivated by some micro- and/or mesoscopic considerations in the optimal case, with a set of material parameters whose values should be distinguishable from sufficiently simple laboratory experiments and/or in situ observations. The first choice for analysing the time-dependent behaviour of materials could be the implementation of generalised viscoelastic

Kelvin chains by [3], working primarily with small-strain simplification and the additive decomposition of strain components.

Further modifications and generalisations of this approach include the following: (a) its extension to creep flow in concrete, as shown in other work (see [4]); (b) the possibility of incorporating additional constitutive components, including those enabling the consistent treatment of plasticity and damage, such as models combining Rankine-type and Hill-type criteria using the mathematical theory of Prandtl–Ishlinskii operators (see [5–8], with the monograph [9]); (c) an analysis of dissipation in viscoelastic architected materials using a representative-volume-element (RVE) framework (see [10]); (d) generalisations required for moving from small-strain to finite-strain formulations and from additive to multiplicative strain decompositions (see [11]). A reasonable compromise between small and finite strain considerations can be achieved through the adaptive update of geometrical descriptions for deformable bodies [12–14]. This approach is particularly effective when applying time discretisation methods (such as the construction of Rothe sequences), facilitating appropriate adaptive remeshing when coupled with the Finite Element Method (FEM) or similar computational techniques.

A reasonable evaluation of contact forces is a crucial tool for the incorporation of (single or multiple) contacts/impacts of deformable bodies into the above-sketched material models; see [15–17], while for the special case of cementitious composites, cf. [18,19]. From the mathematical point of view, we have a weak formulation of an initial and boundary value problem for a certain system of partial differential equations of evolution. The interface conditions connected with contacts/impacts add some nonlinear term, usually in the form of inequalities, whose implementation, particularly time steps, may be a delicate issue. Variants of a penalty approach can be found in the literature. Their basic classification depends on the form of implementation of an FEM-based technique, such as the node-to-segment analysis by [20] (the most frequently used in recent studies, proposing various improvements and modifications), the node-to-node one by [21], and the segment-to-segment one by [22]. Other studies try to overcome the numerical disadvantages of the usual penalty techniques through substantial revision, as in the bi-penalty method by [23], or energy and kinematic approaches, as discussed by [24].

The quality of the energy approaches depends on the proper evaluation of dissipative energy when dealing with contacts/impacts. The proper evaluation of energy loss and its utilisation in the computational predictions of further contact behaviour seems to be an intractable issue. For several types of simplified approaches, see [25–27]; for their need for careful revision in the case of cyclic loads, cf. [28]. Another serious, non-trivial problem consists of the design of a robust, inexpensive, and effective algorithm for the detection of potential interfaces, namely in the case of the expected presence of multiple contacts/impacts; such a design could be based, e.g., on the graph-based neighbour search by [29,30], or on the numerical manifold method (NMM) by [31]. Nevertheless, there are still other challenges in contact mechanics analysis, as introduced by [32], demonstrating the need for a combination of experimental and computational approaches for particular materials and structures. A more detailed description of a (rather simple) possible strategy for modelling contacts will be presented in Section 4.

The research progress in the physical analysis and computational modelling of viscoelastic contacts in recent decades can be found in [33–36]. Recent studies incorporate various formulations of irreversible plasticity and damage at and near contacts/impacts that are in better agreement with observable material behaviour. This can be seen as a stand-alone research area now, beyond the scope of this article. For example, the review article [37] contains 443 references. Remember that, for quasi-brittle materials (including plain and reinforced concrete), one typically observes a progressive transition from (i) the initiation

of microscopic damaged zones to (ii) the formation and growth of macroscopic cracks, and finally to (iii) the complete failure of a material sample or an engineering structure.

Under certain computational simplifications, (i) this can be addressed using non-local smeared-damage formulations that distinguish tensile and compressive responses, usually with a scalar damage variable, or, more rarely and with higher complexity, with a matrix-valued damage variable (see [38,39] for plasticity with damage, refs. [40–43] for the so-called Mazars model with a scalar damage factor, which is open to potential regularisations, and [44,45] for its generalisation to anisotropic damage); (ii) this requires an extension of standard FEM through the enrichment of basis functions along cohesive interfaces, as in XFEM (see [46–49]); (iii) this cannot be reliably predicted without substantial revisions of common physical and geometric idealisations. The mathematical and computational aspects of (i) and (ii) for a viscoelastic model with damage, with brief comments regarding (iii) and highlighting several open issues, are discussed in [50].

Recent works provide promising steps toward addressing (iii), although both the theoretical framework and the corresponding software implementations still require significant further development. A nonlocal gradient damage model for dynamic brittle fracture with a consistent treatment of dissipated energy has been presented in [51]. A nonlocal macro–mesoscale damage (NMMD) model for quasi-brittle materials has been introduced in [52]. The deeper thermodynamic considerations in [53] concerning Helmholtz and Gibbs free energies, dissipation potentials, their subgradients, and related concepts offer a path toward eliminating non-physical parameters from ad hoc constitutive laws.

However, the correct treatment of finite strains requires complementing these ideas with the mathematical theory of structured deformations (see the monograph [54], namely the sections Thermodynamics of selected materials and processes and Evolution at finite strains), together with the recent results of [55]. Even more general formulations, those involving Cosserat continua and their extensions rather than the classical Boltzmann framework, draw upon advanced studies in non-Euclidean geometries and algebraic structures (see [56–58]), whose acceptance in engineering practice (civil, mechanical, etc.) currently remains quite limited.

Drawing from such an extensive research area, this article pays attention only to its rather small part, which is important for the development of advanced computational tools at the Faculty of Civil Engineering in Brno University of Technology, in effective collaboration with the companies FEM Consulting Brno and Dlubal Software Tiefenbach (responsible for the RFEM software package). After this *Introduction* (Section 1), we shall formulate *Physical and Mathematical Preliminaries* (Section 2) for our simplified model problem of the contact/impact of deformable bodies, including potential damage, and continue with *Constitutive Relations* (Section 3), paying attention to different choices of viscoelastic or elastoplastic constitutive equations involving potential damage. Then, the *Computational Examples* (Section 4) demonstrate several benchmark examples to illustrate the advantages and drawbacks of the presented approaches. Finally, the short *Conclusions* (Section 5) summarise the results, along with providing comments on potential applications and significant research challenges.

## 2. Physical and Mathematical Preliminaries

As is usual in many engineering papers, instead of a detailed formulation of the thermodynamic conservation of mass, momentum and energy, and avoiding detailed considerations of thermal changes, we shall start with the equation of motion of a single deformable body, which can be seen as the conservation of momentum in the sense of [59], Part 2.1, compatible with [9], Part 3.2. Note that the formulation based on the conservation of energy will be clearer for some considerations of *Computational Examples*.

We assume that such a body occupies domain  $\Omega$  with its Lipschitzian boundary  $\partial\Omega$  in the three-dimensional Euclidean space  $\mathbb{R}^3$  on a finite time interval  $\mathcal{I} = [0, \zeta]$  (with a potential non-trivial limit passage  $\zeta \rightarrow \infty$ ). Domain  $\Omega$  is supplied by the Cartesian coordinate system  $x = (x_1, x_2, x_3)$ , where  $t$  denotes a time from  $\mathcal{I}$ , and dot symbols are used instead of  $\partial/\partial t$  for brevity. The boundary  $\partial\Omega$  consists of two disjointed parts  $\Theta$  (for Dirichlet boundary conditions) and  $\Gamma$  (for Neumann boundary conditions).

To simplify the further formulae, let us introduce the following notations:

$$(\phi, \psi) = \sum_{i=1}^3 \int_{\Omega} \phi_i(x) \psi_i(x) dx \quad (1)$$

for appropriate functions  $\phi(x) = (\phi_1(x), \phi_2(x), \phi_3(x))$ ,  $\psi(x) = (\psi_1(x), \psi_2(x), \psi_3(x))$  of arguments  $x \in \Omega$ ,

$$(\phi, \psi) = \sum_{i=1}^3 \int_{\Gamma} \phi_i(x) \psi_i(x) ds(x) \quad (2)$$

for appropriate functions  $\phi(x) = (\phi_1(x), \phi_2(x), \phi_3(x))$ ,  $\psi(x) = (\psi_1(x), \psi_2(x), \psi_3(x))$  of arguments  $x \in \Gamma$  and

$$(\phi, \psi) = \sum_{i,j=1}^3 \int_{\Gamma} \phi_{ij}(x) \psi_{ij}(x) dx \quad (3)$$

for appropriate matrices  $\phi(x)$  and  $\psi(x)$  compounded from functions  $\phi_{ij}(x)$  and  $\psi_{ij}(x)$  with  $i, j \in \{1, 2, 3\}$  of arguments  $x \in \Omega$ . Taking (1)–(3) into account, the equation of motion for any  $t \in \mathcal{I}$  reads

$$(v, \rho \ddot{u}) + (v, \rho \dot{u}) + ((\varepsilon(v), \sigma)) = (v, f) + \langle v, g \rangle \quad (4)$$

where  $v(x) = (v_1(x), v_2(x), v_3(x))$  denotes arbitrary virtual displacements related to the reference configuration for  $t = 0$ ;  $\varepsilon(w(x))$  means the linearised tensor for any admissible argument  $w$  in the usual sense  $\varepsilon_{ij}(w(x)) = (\partial w_i(x)/\partial x_j + \partial w_j(x)/\partial x_i)/2$  with  $i, j \in \{1, 2, 3\}$  (for  $w(x, t)$ , this can be repeated with a fixed  $t$  similarly);  $\sigma$  analogously refers to the stress tensor;  $g(x, t) = (g_1(x, t), g_2(x, t), g_3(x, t))$  denote the prescribed surface loads of  $\Gamma$  (discrete loads here and later, which can be implemented using the Dirac distributions), whereas  $f(x, t) = (f_1(x, t), f_2(x, t), f_3(x, t))$  means the prescribed volume loads on  $\Omega$ . All supports are characterised by  $v(x) = \mathcal{O}$  for  $x \in \Omega$ , where, formally,  $\mathcal{O} = (0, 0, 0)$ .

Moreover, (4) contains two real material characteristics: the positive material density  $\rho(x)$  and the non-negative mass damping factor  $\zeta(x)$  with  $x \in \Omega$ . Two Cauchy initial conditions,  $u(x, 0) = \mathcal{O}$  and  $\dot{u}(x, 0) = \mathcal{O}$ , for all  $x \in \Omega$  will be considered for simplicity. Our aim is then to find  $u(x, t)$  satisfying (4). Clearly, this setting requires some reasonable formulation of constitutive strain–stress relation(s) between  $\sigma$  and  $\varepsilon(u)$ , which will be discussed in Section 3.

From the mathematical perspective, (4) with the above-introduced initial conditions can be understood as an initial and boundary value problem for a weak formulation of a hyperbolic partial differential equation of evolution. Its usual nonlinearity (except linear elasticity) depends on the equations and/or inequalities characterising the dependence of  $\sigma$  on  $u$ . Applying the standard notation of Lebesgue, Sobolev, Bochner–Sobolev, etc., and the (abstract) function spaces by [60,61], it is reasonable to assume  $\rho, \zeta \in \mathcal{Z}$ ,  $\zeta \in \mathcal{Z}$  with  $\mathcal{Z} = L^\infty(\Omega)$ ,  $f \in L^2(\mathcal{I}, \mathcal{H})$  with  $\mathcal{H} = L^2(\Omega)^3$ ,  $g \in L^2(\mathcal{I}, \mathcal{G})$  with  $\mathcal{G} = L^2(\Omega)^3$ ,  $\sigma \in L^2(\mathcal{I}, \mathcal{E})$  with  $\mathcal{E} = L^2_{\text{sym}}(\Omega)^{3 \times 3}$  and any  $v \in \mathcal{V}$  with  $\mathcal{V} = \{w \in W^{2,2,2}(\mathcal{I}, \mathcal{V}, \mathcal{H}, \mathcal{V}^*) : w(x) = \mathcal{O} \text{ for } x \in \Omega\}$ ,  $\mathcal{V}^*$  being an adjoint space to  $\mathcal{V}$ . Clearly, in this case, (1) can be understood as a scalar product in  $\mathcal{H}$ , (2) as that in  $\mathcal{G}$ , and (3) as that in  $\mathcal{E}$ ; in more general spaces, (1)–(3) can still be taken as certain dualities between original and adjoint spaces. The strategy of verification of the existence of a solution  $u$ , using the method of discretisation

in time and the properties of several types of Rothe sequences, depends on the presence of various nonlinearities in the constitutive relations; cf. [62] with micro- and macroscopic damage considerations.

From the computational perspective, the method of discretisation in time converts an original hyperbolic problem (4) on  $\mathcal{I}$  to a sequence of elliptic problems in discrete times that are typically still in infinite-dimensional spaces and not suitable for practical calculations; thus, an additional discretisation on  $\Omega$ ,  $\Theta$ , and  $\Gamma$  is needed to obtain a finite system of (frequently nonlinear) algebraic equations using a finite element or similar techniques or their modifications. Another way to arrive at a comparable system could be based on the Fourier multiplicative decomposition, inspired by [59], Part 3.3: taking  $u_i(x, t)$  with  $i \in \{1, 2, 3\}$  as the infinite series  $\sum_{j=1}^n \varphi_j(x) \mathcal{U}_{ij}(t)$  for a finite integer  $n$  (admitting the limit passage  $n \rightarrow \infty$ ) and a priori-prepared linearly independent functions  $\varphi_1(x), \dots, \varphi_n(x)$ , zero-valued on  $\Theta$  (or its suitable approximation), one can see easily that (1) generates a finite system of ordinary differential equations

$$\mathcal{M}\ddot{U} + \mathcal{C}\dot{U} + \tilde{\mathcal{F}}(U) = \mathcal{F} \quad (5)$$

with some symmetric square matrices  $\mathcal{M}$  and  $\mathcal{C}$ , a vector of all discretised external loads  $\mathcal{F}$  and some vector function  $\tilde{\mathcal{F}}(U)$ , representing internal forces. Differentiating  $\tilde{\mathcal{F}}(U) = \tilde{\mathcal{F}}'(U)U = \mathcal{K}(U)U$ , with a new (stiffness) matrix  $\mathcal{K}(U)$ , from (5), we receive

$$\mathcal{M}\ddot{U} + \mathcal{C}\dot{U} + \mathcal{K}(U)U = \mathcal{F}. \quad (6)$$

or a hypothetical  $\mathcal{K}$  independent of  $U$ ; this leads to the generalised eigenvalue analysis, without any discretisation in time. Taking  $\mathcal{V} = \dot{U}$ , (6) can be rewritten, e.g.,

$$\begin{bmatrix} \mathcal{M} & \mathcal{C} \\ \mathfrak{D} & \mathcal{M} \end{bmatrix} \cdot \begin{bmatrix} \dot{\mathcal{V}} \\ \dot{U} \end{bmatrix} + \begin{bmatrix} \mathfrak{D} & \mathcal{K}(U) \\ -\mathcal{M} & \mathfrak{D} \end{bmatrix} \cdot \begin{bmatrix} \mathcal{V} \\ U \end{bmatrix} = \begin{bmatrix} \mathcal{F} \\ o \end{bmatrix} \quad (7)$$

where  $\mathfrak{D}$  is a square matrix and  $o$  a vector of corresponding size. A time-discretised form of (7)

$$\begin{bmatrix} \mathcal{M} & \mathcal{C} \\ \mathfrak{D} & \mathcal{M} \end{bmatrix} \cdot \begin{bmatrix} \mathcal{V}_s - \mathcal{V}_{s-1} \\ \mathcal{U}_s - \mathcal{U}_{s-1} \end{bmatrix} + h \begin{bmatrix} \mathfrak{D} & \mathcal{K}(\mathcal{U}_s^*) \\ -\mathcal{M} & \mathfrak{D} \end{bmatrix} \cdot \begin{bmatrix} \mathcal{V}_s \\ \mathcal{U}_{sas} \end{bmatrix} = h \begin{bmatrix} \mathcal{F}_s \\ o \end{bmatrix} \quad (8)$$

for an integer  $m$  ( $m \rightarrow \infty$  theoretically),  $s \in \{1, \dots, m\}$ ,  $h = \zeta/m$  generates a sparse system of linear algebraic equations for unknown  $(\mathcal{U}_s, \mathcal{V}_s)$ , inserting  $\mathcal{U}_s^* = \mathcal{U}_{s-1}$  as the first estimate. The update of  $\mathcal{U}_s^*$  in (8) can then be used for the iterative improvement of  $\mathcal{U}_s$ .

Fortunately, most of these considerations can be repeated for a finite number of deformable bodies with potential contact surfaces; some adaptive remeshing strategy, e.g., that motivated by [13], may be needed for the effective handling of problems with large deformation. Let us consider two deformable bodies in the following comments for brevity; their formal extension to a finite number of deformable bodies is straightforward, unlike the difficult computational identification of real multiple contacts, cf. [62]. Let  $\Lambda$  be a potential contact surface between such two bodies  $\Omega_1$  and  $\Omega_2$ . Then, it is sufficient to extend (5), composed from terms inherited from both  $\Omega_1$  and  $\Omega_2$ , by a right-side term  $\langle [v], p \rangle_*$ , similar to  $\langle v, g \rangle$ , with the star in the index referring to  $\Lambda$  instead of  $\Gamma$ ; outward unit normals  $\mathfrak{N}$  to  $\Lambda$  from  $\Omega_1$  and  $\Omega_2$  have opposite orientations. The evaluation of  $p$  from the jumps  $\delta u$  (in the sense of traces) between  $u$  coming from  $\Omega_1$  and  $\Omega_2$  is required;  $\delta v$  can be introduced similarly. In the following considerations,  $|\cdot|$  means the Euclidean norm and  $\cdot$  the corresponding scalar product in  $\mathbb{R}^3$  for brevity. The normal and tangential components of  $u$  are  $u^{\mathfrak{N}} = (u \cdot \mathfrak{N})\mathfrak{N}$  and  $u^\tau = u - u^{\mathfrak{N}}$ ; moreover, it is useful to define  $\mathfrak{E} = u^\tau / |u^\tau|$ . The

(normal) impenetrability condition on all contact candidates  $\Lambda$  reads  $u^{\text{nt}} \geq 0$ ; real contact occurs only in the case  $u^{\text{nt}} = 0$ , where  $p = \mathcal{P}_\tau(\cdot, |u^\tau|)\mathfrak{E}$ ,  $\mathcal{P}$  being an appropriate function of  $|u^\tau|$ , taking the (tangential) friction into account; its first parameter is reserved for  $x \in \Lambda$  to admit different levels of friction at particular points of  $\Lambda$ , as an additional material characteristic of  $\Lambda$ . The way from (5) to (6)–(8) can then be followed with obvious formal modifications; for a more detailed discussion of this and several alternative computational approaches, see [24]. However, the proper mathematical treatment of their formulae needs (in general) the analysis of nonlinear integral inequalities, the application of Carathéodory properties, Nemytskii mappings, etc.

Notice that (5), including the last extension, does not correspond to a closed physical system in general because (at least) two sources of energy dissipation can be distinguished there: the second left-hand-side additive term of (4) (except  $\zeta = 0$  everywhere) and the just-discussed friction term on  $\Lambda$  (except no contact occurs or  $\mathcal{P}$  is always zero-valued). Nevertheless, the most significant source of energy dissipation in structural engineering problems usually comes from the strain–stress relations, as discussed in the following section.

### 3. Constitutive Relations

To complete the integral Equation (6), we must formulate appropriate constitutive equations between the total stress  $\sigma \in L^2(\mathcal{I}, \mathcal{E})$  and the strain  $\varepsilon(u)$ , which are valid on  $\Omega$ , applicable at any time  $t \in \mathcal{I}$ . Let us ignore all considerations of the last two paragraphs of the preceding section, which bring complications of another type, for simplicity. The simplest choice is the linear dependence, well-known as Hooke law,  $\sigma = \mathfrak{C}\varepsilon(u)$ , where  $\mathfrak{C}$  is the fourth-order tensor from  $L^2(\Omega)_{\text{sym}}^{(3 \times 3) \times (3 \times 3)}$  such that  $\mathfrak{A}^T \mathfrak{C}(x) \mathfrak{A} \geq c \mathfrak{A}^T \mathfrak{A}$  for an arbitrary matrix  $\mathfrak{A} \in \mathbb{R}_{\text{sym}}^{3 \times 3}$  and a certain positive constant  $c$ . Remember that in the isotropic case,  $\mathfrak{C}$  can be compounded from two Lamé constants only, or from the Young modulus  $E$  and the Poisson ratio  $\nu$ . Then, (5)–(8) can be rewritten literally with a constant  $\mathcal{K}$ . In the case of the preferred method being discretisation in time, we can rewrite (4) as

$$(v, \rho \mathcal{D}^2 u_s^m) + (v, \zeta \rho \mathcal{D} u_s^m) + ((\varepsilon(v), \mathfrak{C}\varepsilon(u_s^m))) = (v, f_s^m) + \langle v, g_s^m \rangle \quad (9)$$

with  $\mathcal{D} u_s^m = (u_s^m - u_{s-1}^m)/h$  and  $\mathcal{D}^2 u_s^m = (\mathcal{D} u_s^m - \mathcal{D} u_{s-1}^m)/h$  for  $s \in \{1, \dots, m\}$ ; here,  $u_{-1} = u_0 = 0$  (due to the Cauchy initial conditions). While  $f_s^m$  and  $g_s^m$  can be taken, e.g., as the Clément quasi-interpolations by [60]. In part 8.2,  $u_s^m$  and  $u_{s-1}^m + (t - (s-1)h) \mathcal{D} u_s^m$  for  $(s-1)h < t \leq sh$  generate two types of the so-called Rothe sequences: of simple (abstract) functions in the first case and of linear Lagrange splines in the second one. Consequently, the linear existence and convergence results are available in the standard textbooks on linear functional analysis, namely the Lax–Milgram theorem by [63] (for an elliptic equation, i.e., for a static case, and also for (9) for a fixed  $s$ ) and for the a priori bound and convergence properties of Rothe sequences by [64] (for a hyperbolic equation, i.e., for a dynamic case).

The obvious first generalisation relies on the implementation of the Kelvin–Voigt parallel viscoelastic model using a new positive material factor  $\alpha \in \mathcal{Z}$ ; this is a new source of energy dissipation, known as structural damping (unlike the mass damping introduced in (4)) in most analyses in structural engineering. Since  $\sigma = \alpha \mathfrak{C}\varepsilon(\dot{u}) + \mathfrak{C}\varepsilon(u)$  in (4) in this case, the third left-hand-side additive term in (9) is only extended to  $((\varepsilon(v), \alpha \mathfrak{C}\varepsilon(\mathcal{D} u_s^m))) + ((\varepsilon(v), \mathfrak{C}\varepsilon(u_s^m)))$  without loss of linearity; for the concurrent Maxwell serial viscoelastic model and various combinations of parallel and serial models, including the derivation of some explicit (both differential and integral) computational formulae; see [3]. Here, we present, as a model case, only the so-called standard linear solid model (SLS) corresponding to Figure 1; an additional positive material factor  $\beta \in \mathcal{Z}$  is needed here.

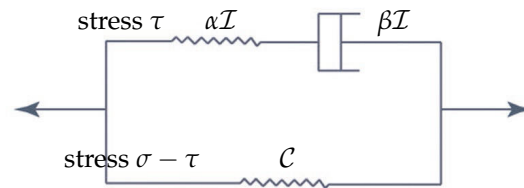


Figure 1. Engineering scheme of the viscoelastic SLS model.

A model problem, inspired by the deeper (predominantly quasi-static) analysis of selected viscoelastic problems by [50], analogous to (9), with the expectable limit passage  $m \rightarrow \infty$ , reads

$$\begin{aligned} ((\varepsilon(v), \tau_s^m)) + (v, \rho \mathcal{D}^2 u_s^m) + (v, \zeta \rho \mathcal{D} u_s^m) + ((\varepsilon(v), \mathfrak{C} \varepsilon(u_s^m))) &= (v, f_s^m) + \langle v, g_s^m \rangle, \quad (10) \\ ((\gamma, \mathfrak{C}^{-1} \tau_s^m / \alpha)) + h((\gamma, \mathfrak{C}^{-1} (\tau_1^m + \dots + \tau_s^m) / \beta)) &= ((\gamma, \varepsilon(u_s^m))) \end{aligned}$$

for arbitrary  $v \in \mathcal{V}$  and  $\gamma \in \mathcal{G}$ . Note that both cases with missing terms  $\alpha \mathfrak{C}$  and  $\beta \mathfrak{C}$  by Figure 1, corresponding to the classical Kelvin and Maxwell models, have to be discussed separately. Fortunately, the above-mentioned linearity is still preserved; thus, the linear functional analysis is available, and we still come, after the additional discretisation on  $\Omega$ ,  $\Theta$ , and  $\Gamma$ , to certain sparse systems of linear algebraic equations in practical calculations.

However, such calculations cannot produce reasonable results for materials with different damage behaviours under tension and compression, namely the estimate of the dangerous loss of stiffness caused by the development of microscopic damage. A seemingly simple remedy is the replacement of  $\mathfrak{C}$  in the third left-hand-side additive term in the first equation of (10) by certain  $(1 - \mathfrak{D})\mathfrak{C}$ , with  $\mathfrak{D}$  understood as a damage factor with values between 0 and 1; for  $t = 0$ , usually with  $\mathfrak{D} = 0$  (no initial damage occurs). The adequate change should also be made in the lower branch of Figure 1, also with  $(1 - \mathfrak{D})\mathfrak{C}$  instead of  $\mathfrak{C}$ . We cannot expect reasonable results for case (iii) in the *Introduction* from such a simplified formulation; thus,  $\mathfrak{D} < 1$  has to be controlled. In general, to reflect the irreversibility of damage,  $\mathfrak{D}$  must be non-decreasing in  $t$ . An evaluation can be conducted for appropriate strain invariants to guarantee the independence of the choice of Cartesian coordinates; however, we can write  $\mathfrak{D}(u_s^m)$  formally. This imports an unpleasant nonlinearity into the first equation of (10) (unlike the second one). Fortunately, using the assumptions contained in the cautious five-step algorithm of the non-local evaluation of  $\mathfrak{D}$  by [62], the solvability of a quasi-linear system (10) for a fixed  $s \in \{1, \dots, m\}$  can be guaranteed using another classical result by [65]; consequently, the technique based on the analysis of (more types of special) Rothe sequences can be applied again successfully. Nevertheless, the convergence of an iterative computational linearisation, inspired by (8), based on the replacement of  $\mathfrak{D}(u_s^m)$  by certain  $\mathfrak{D}(u_s^{m*})$ , using the first estimate  $\mathfrak{D}(u_s^{m*}) = \mathfrak{D}(u_{s-1}^m)$ , must be verified separately, due to the (frequently complicated) form of  $\mathfrak{D}(\cdot)$ .

Really, the need to know a lot of complicated material functions that are contained in such an algorithm, whose laboratory identification is nearly impossible, leads to the still-persisting discrepancy between formal mathematical verification and reasonable engineering computations. For cementitious composites, including concrete, numerous authors implement the so-called Mazars model from [40], revisited by [41], or some slight modification of it, whose main ideas will be sketched now. In its original form, no non-zero initial strain–stress relation relies on (9), where no non-zero  $\alpha$  or  $\beta$ , introduced by Figure 1, are needed. Namely, ref. [41] starts with the evaluation of the triple eigenvalues of  $(\varepsilon_1, \varepsilon_2, \varepsilon_3)$  of a matrix  $\varepsilon(v)$  for any  $v \in \mathcal{V}$ . Setting  $v = u_s^m$  by (10), we are able to derive two strain invariants (no time step indices are presented for the sake of notation simplicity)

$I_\varepsilon = \varepsilon_1 + \varepsilon_2 + \varepsilon_3$  and  $2J_\varepsilon = (\varepsilon_1 - \varepsilon_2)^2 + (\varepsilon_2 - \varepsilon_3)^2 + (\varepsilon_3 - \varepsilon_1)^2$ ; these are useful for the evaluation of two equivalent strain characteristics

$$\varepsilon_t = \frac{I_\varepsilon}{2(1-2\nu)} + \frac{\sqrt{J_\varepsilon}}{2(1+\nu)}, \quad \varepsilon_c = \frac{I_\varepsilon}{5(1-2\nu)} + \frac{6\sqrt{J_\varepsilon}}{5(1+\nu)} \quad (11)$$

for cracking and crushing. To force the irreversibility of damage, one must take the maxima  $\varepsilon_t^*, \varepsilon_c^*$  from  $\varepsilon_t, \varepsilon_c$  by (11) in all previous time steps, starting from certain initial thresholds  $\varepsilon_t^0, \varepsilon_c^0$ . The evaluation of the  $\varepsilon^* = r\varepsilon_t^* + (1-r)\varepsilon_c^*$  then needs the triaxial factor

$$r = \frac{\max(\tilde{\sigma}_1, 0) + \max(\tilde{\sigma}_2, 0) + \max(\tilde{\sigma}_3, 0)}{|\tilde{\sigma}_1| + |\tilde{\sigma}_2| + |\tilde{\sigma}_3|}, \quad (12)$$

derived from the triple of the eigenvalues  $(\tilde{\sigma}_1, \tilde{\sigma}_2, \tilde{\sigma}_3)$  of  $\tilde{\sigma} = \mathcal{C}\varepsilon(u_s^m)$ , i.e.,  $\tilde{\sigma} = \sigma_s^m / (1 - \mathfrak{D}(u_s^m))$  in the modification of (9) with  $1 - \mathfrak{D}(u_s^m)\mathcal{C}\varepsilon(u_s^m)$  instead of  $\mathcal{C}\varepsilon(u_s^m)$ . Finally, we have

$$\mathfrak{D} = 1 - \frac{(1-A)\varepsilon_0^*}{\varepsilon^*} - A \exp(-B(\varepsilon^* - \varepsilon_0^*)) \quad (13)$$

with certain material parameters,  $A$  and  $B$ , coming from the compression and tension, or flexural bending tests,  $\varepsilon_0^*$  being the initial threshold for  $\varepsilon^*$ . Later studies [42,43] require additional regularisation for some evaluations, like (11)–(13), etc., which may correspond to the nonlocal approach needed in [62].

As an alternative approach, avoiding all viscoelastic models, a special choice of yield functions (surfaces) in the standard theory of plasticity, coupled with pure elasticity (usually linear, as before), is available to express the different material behaviours under tension and compression and to implement a certain type of energy dissipation. A simple additive decomposition of the strain tensor  $\varepsilon(\cdot) = \varepsilon_e(\cdot) + \varepsilon_p(\cdot)$  (still working with the small strain theory) can be applied, where  $\mathcal{C}\varepsilon_e(\cdot) = \sigma$  and  $\dot{\varepsilon}_p(\cdot) = \dot{\kappa} \partial\psi / \partial\sigma$ , using the plastic potential  $\psi$ . Yielding can occur only in cases where the general yield criterion  $\phi(\sigma, \bar{\sigma}(\kappa)) = 0$  is satisfied by  $\sigma$ ; here,  $\bar{\sigma}$  is a function of a scalar  $\kappa$ , introduced as a certain measure of inelastic straining. Both loading and unloading can be described by the Karush-Kuhn-Tucker triple of conditions of the type  $\dot{\kappa}\phi = 0, \phi \geq 0, \dot{\kappa} \leq 0$ . The adequate evaluation of  $\phi, \psi$ , and  $\bar{\sigma}$  for two-dimensional problems and orthotropic materials is presented as a Rankine-type criterion for tensile strength, coupled with a Hill-type criterion for compressive strength, in the work of [6] in great detail, including the iterative evaluation of  $\varepsilon(\cdot)$ . This is illustrated by Figure 2, using the classical notation  $\sigma_1$  and  $\sigma_2$  for principal stresses,  $f_{ct}$  for tensile strength, and  $f_{cc}$  for yield stress. In this case, the von Mises criterion was shown to represent the isotropic version of the Rankine–Hill material model when shear stress  $\tau = 0$ . The intuitive three-dimensional (less transparent) generalisation of this approach is developed in [7]. Note that the evaluation of smeared damage and plastic strain can be coupled, as demonstrated by [8].

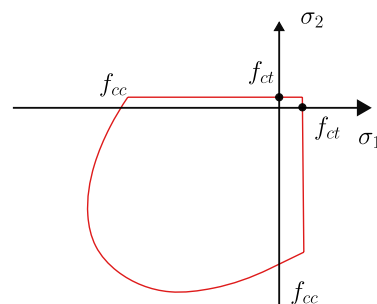


**Figure 2.** Special composite yield functions for the Rankine–Hill plasticity, in its isotropic variant, used throughout the presented article.

Although all constitutive relations discussed in this section are related to case (i), mentioned in the *Introduction*, its coupling with case (ii) is also possible, cf. [62]. Instead of a single domain  $\Omega$ , let us consider a union of these particular domains, separated by their interfaces  $\Psi$ . The initiation and development of macroscopic cracks can then be driven by a certain traction separation law, bringing a new nonlinear term  $\langle v, \mathcal{T} \rangle_{\times}$  to (4), where  $\times$  refers to  $\Psi$  instead of  $\Gamma$  and an additional constitutive relation of the type  $\mathcal{T} = \varpi(\cdot, Du)$  must be supplied:  $D$  refers again to the jumps (in the sense of traces); the first parameter should enable the inhomogeneity of interfaces, and some a priori known function  $\varpi$ , measurable in the first argument on  $\Psi$  and continuous in the second one, should be supplied to avoid difficulties in both its physical interpretation and mathematical proofs. The full discretisation requires some modification of the standard finite element technique, related to the initiation and development of damage on  $\Psi$  as the (improved) extended finite element method (XFEM) by [46]; moreover, various singular phenomena on crack tips must be handled separately using certain integral stress intensity factors by [48].

#### 4. Computational Examples

All numerical calculations presented in this article rely on the solver created by the company FEM Consulting Ltd in Brno. To demonstrate the need for a deeper study of dissipative energy in the numerical modelling of the contact/impact of deformable bodies, two examples will be presented here: (1) the benchmark one, with two bodies, where the first is falling on the second, supported at the bottom; (2) the impact of a steel punch on a reinforced concrete beam, motivated by the unresolved problems encountered during the solution of the project of the Ministry of Industry and Trade of the Czech Republic *The software tool for the nonlinear analysis of concrete structures during fast dynamic processes* (No. FV20372, 2017–2020, I. Němec et al.); cf. [66]. For both cases, three basic types of material models were chosen for comparison: (a) the Kelvin–Voigt viscoelastic material model, (b) the elastoplastic model applying the Rankine–Hill criterion, and (c) the Mazars damage model. Various definitions of (a), (b), and (c), as well as their generalisations, sketched in the previous section, are available.

For the time integration, the (sufficiently simple) Euler backward method was preferred everywhere, with adaptive time steps due to numerical demands and the size of the finite element mesh. Since both numerical examples, (1) and (2), work mainly with a shell finite element type, the contact between two bodies was considered a line-to-line contact. This requires careful control of the time integration steps and forces appropriate modifications in (10), which is more suitable for mathematical proofs (to demonstrate the formal convergence of sequences of approximate solutions in Sobolev–Bochner spaces independent of the choice of discretisation in  $\mathbb{R}^3$ ) than for practical calculations.

The kinematic method used for the calculation of contact and impact problems is a non-traditional approach that is specifically tailored to use with the explicit time integration schemes, as an alternative to methods like the penalty method; for more details, see [24]. The fundamental principle of the kinematic method is that it exactly satisfies the condition of impenetrability of colliding bodies, meaning that the union of the two deformable bodies, represented by domains  $\Omega_1$  and  $\Omega_2$ , must be empty. This method is regarded as superior to the penalty method due to its high accuracy, efficiency, and robustness, and because it avoids relying on computational parameters such as penalty stiffness factors or Lagrangian multipliers. The approach operates based on basic kinematic principles and the law of conservation of momentum.

When implemented in explicit time stepping, the kinematic method does not calculate contact forces as separate variables. Instead, it enforces a correction of nodal displacement at all potential interfaces. The core operational steps include first precisely calculating the

exact collision time  $t_c$ . The indices  $k \in \{A, B, C, D\}$ , where said letters refer to the borders of deformable bodies, typically denote the nodes or points involved in the collision. The position vector of a point  $k$  at time  $t$  is generally given by  $x_k(t) = x_k(0) + tv_k$ , where  $x_k(0)$  is the initial position vector and  $v_k$  is the assumed constant velocity vector during the time step. For node D striking a surface triangle  $ABC$ , time  $t_c$  is found by solving the cubic equation  $C_3t_c^3 + C_2t_c^2 + C_1t_c + C_0 = 0$ , where  $C_0, C_1, C_2$ , and  $C_3$  are the coefficients derived from the condition that the points must lie in the same plane at impact. The smallest positive solution  $t_c$  that does not exceed computational time step  $\Delta t$  is selected. Second, the standard computational time step  $\Delta t$  must be decomposed into two sub-intervals using the known time points  $t_n$  and  $t_{n+1}$  with a certain integer  $n$ : the time before impact and the time immediately following impact, e.g.,  $t_n < t_c \leq t_{n+1}$ . In the following considerations,  $\Delta$  will be used for the differences in values at  $t_n$  and  $t_{n+1}$  for brevity.

Next, the kinematic correction is applied during the post-impact interval from  $t_c$  to  $t_{n+1}$ , assuming a perfectly inelastic collision. This ensures the colliding parts move at the same speed in the direction of the collision after the impact. The kinematic approach utilises the conservation of linear and angular momentum. For a simple node-to-node contact, the new velocity  $v_{1,2}^{\text{new}}$  is calculated by dividing the sum of the momenta  $p_1 + p_2$  by their combined mass  $m_1 + m_2$  as  $v_{1,2}^{\text{new}} = (p_1 + p_2)/(m_1 + m_2)$ , where  $p_1$  and  $p_2$  are the momenta and  $m_1$  and  $m_2$  are the respective masses of the two nodes. For the more general node-to-segment contact, the slave node momentum  $p_3$  is distributed to the master nodes (1 and 2) based on the interpolation coefficients  $\xi$  and  $1 - \xi$ . The resulting new velocities for the master nodes are calculated, such as  $v_{1,t_{n+1}}^{\text{new}} = (p_1 + (1 - \xi)p_3)/(m_1 + (1 - \xi)m_3)$  and  $v_{2,t_{n+1}}^{\text{new}} = (p_2 + \xi p_3)/(m_2 + \xi m_3)$ , ensuring that the total momentum  $p$  remains constant, meaning the change in total momentum  $p$  is zero.

The method incorporates friction by considering two theoretical limits—absolute friction ( $\beta = 1$ ) and zero friction ( $\beta = 0$ )—where  $\beta$  is the friction coefficient. General friction cases  $0 \leq \beta \leq 1$  are solved by interpolating the final post-impact velocity  $v^\times$  between the absolute friction solution  $v_k^{\text{a}\times\text{*}}$  and the zero-friction solution  $v_k^{\text{z}\times\text{*}}$  using the relation  $v^\times = \beta v_k^{\text{a}\times\text{*}} + (1 - \beta)v_k^{\text{z}\times\text{*}}$  for all  $k \in \{A, B, C, D\}$ . Finally, the nodal coordinates are adjusted using the known velocities and the split time intervals to determine the final position  $x_k^\times$ , often using a weight factor  $w$  between 0 and 1 (often  $w = \frac{1}{2}$ ) via the following equation:  $x_k^\times = x_k + wt_c v_k + (1 - w)t_c v_k^\times$ .

The calculation of the total dissipative energy of the element  $W_{\text{diss,total}}$  was initiated at the level of the integration Gauss points. In each time step (from  $n$  to  $n + 1$ ), the dissipative energy per unit volume  $\Delta W_{\text{diss}}$  was determined by summing the increments of energy dissipation from every active physical process inherent to the specific material model. This approach ensured that the total non-recoverable energy loss was accurately attributed to its physical source.

Three fundamental dissipative energy increments, calculated using the trapezoidal rule on inelastic components, were defined and used as follows. Plastic dissipation  $\Delta W_p$  was associated with irreversible plastic strain and was computed using the average stress acting on the plastic strain increment,  $\Delta W_p \approx \frac{1}{2}(\sigma^n + \sigma^{n+1}) : \Delta \varepsilon^p$ , containing  $\sigma^n$ ,  $\sigma^{n+1}$  and  $\Delta \varepsilon^p$  with values in  $\mathbb{R}_{\text{sym}}^{3 \times 3}$ , with the symbol: referring to the standard scalar product in  $\mathbb{R}^{3 \times 3}$ . Furthermore, damage dissipation  $\Delta W_d$  was linked to the evolution of the scalar damage variable  $d$  and was calculated using the thermodynamic force  $Y$  conjugate to  $d$ , where  $\Delta W_d \approx \frac{1}{2}(Y^n + Y^{n+1})\Delta d$ . Lastly, viscous dissipation,  $\Delta W_v$ , was associated with the strain rate  $\dot{\varepsilon}$  in the viscous component and was approximated as the work performed by viscosity  $\eta$  in the form  $\Delta W_v \approx \int_{t_n}^{t_{n+1}} \dot{\varepsilon} : \eta : \dot{\varepsilon} dt = \Delta t \left( \frac{\Delta \varepsilon}{\Delta t} \right) : \eta : \left( \frac{\Delta \varepsilon}{\Delta t} \right) = \frac{\Delta \varepsilon : \eta : \Delta \varepsilon}{\Delta t}$ .

For any given material model, the total dissipative energy increment at a Gauss point was the sum of only the relevant (active) terms:  $\Delta W_{\text{diss}} = \Delta W_p + \Delta W_d + \Delta W_v$ .

For instance, for the Kelvin–Voigt viscoelastic model, the dissipation was purely viscous, i.e.,  $\Delta W_{\text{diss}} = \Delta W_v$ , the Rankine–Hill elastoplastic model included only plastic dissipation in the form  $\Delta W_{\text{diss}} = \Delta W_p$  and the Mazars damage model focused purely on damage dissipation  $\Delta W_{\text{diss}} = \Delta W_d$ . Finally, the total dissipative energy for the entire element  $W_{\text{diss,total}}$  was calculated by performing a numerical integration (summation) of the contributions from the Gauss points:  $W_{\text{diss,total}}^{n+1} = W_{\text{diss,total}}^n + \sum_b \Delta W_{\text{diss},b}^n V_b$ , where  $\Delta W_{\text{diss},b}$  was the increment of dissipative energy at a particular Gauss point  $b$  (the sum over all such points was considered) and  $V_b$  was the corresponding integration factor. For its significance in a real engineering structure, see [67].

Through omitting the left-hand-side term in the upper branch in Figure 1 (i.e.,  $\alpha$  is not needed) and taking  $\beta C_I$  instead of  $\beta C$  for simplicity, with  $C_I$  being the identity mapping, evaluated in the same physical units as  $C$ , in its right-hand-side term, we are able to set  $\beta = 10^6$ . Such a choice, together with  $\zeta = 0$  in all cases, cf. (4), then corresponds to a damping of approximately 2–3% for calculated structures.

For the purposes of this comparative study, two examples were created whose dissipated energy was then calculated. The first one, serving as a benchmark for testing the correctness of our algorithms, is the impact of a steel body on a concrete block, as shown in Figure 3. The smaller block is also supported in its corners using nodal supports, which ensures it only travels along the global vertical axis. The material parameters for the impacting block (considered for homogeneous and isotropic bodies) were  $E = 210$  GPa and  $\nu = 0.3$ , which correspond to steel class S235 from Eurocode and bilinearized concrete diagram, which approximately represents concrete C30/37 for the bottom block. Both blocks were modelled using shell finite elements and their thicknesses were chosen as 400 mm for the concrete one and 200 mm for the steel one. For such a choice, the sensitivity of numerical analysis on mesh size setting could be studied. To determine its significance on a real engineering structure, see [67]. However, advanced sensitivity evaluations may be rather complicated, even for benchmark problems; cf. [68].

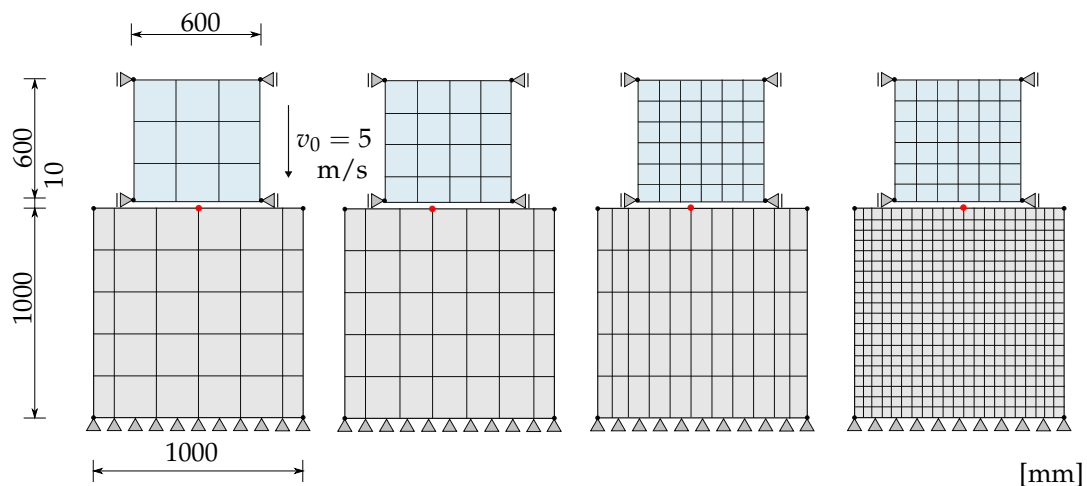


**Figure 3.** Structural scheme of a benchmark example—an impacting steel body on a bigger concrete block with various mesh sizes (0.2 m, 0.15 m, 0.1 m, 0.05 m). For the steel block, a linear elastic material model was used, while for the concrete block, a bilinearized concrete diagram was employed; see Figure 4.

To reflect the realistic behaviour of concrete in the second example, computational simulations work with the stress–strain diagram obtained from the site tests; see Figure 4. Unlike (1), (2) represents a more practical case of a loading test of a reinforced concrete beam loaded by a free-fall of a steel punch. Both the beam and the steel punch are modelled using shell elements, with the reinforcement simplified as beams. The concrete beam itself

is 1.7 m tall, with a height of 0.25 m and thickness 0.2 m; it is supported on both sides by a rigid line support that is inactive in the negative vertical direction to allow the beam to leap up after the punch's impact; see Figure 5. The length of the line support is 0.23 m on each side. The steel punch itself is 0.2 m wide with a length 0.8 m and thickness 0.4 m, and its centre is located directly above the middle of this beam. Two reinforcement bars with a diameter of 10 mm are placed at the top and at the bottom of the beam.

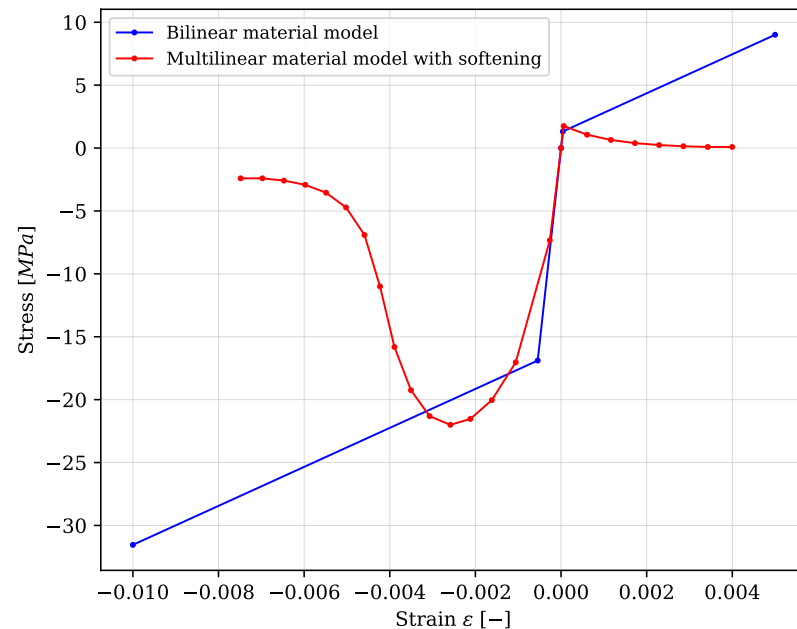


**Figure 4.** Stress–strain diagram representing the concrete C30/37. Red line represents measured concrete properties, blue line represents a bilinear simplification with hardening for the benchmark example.

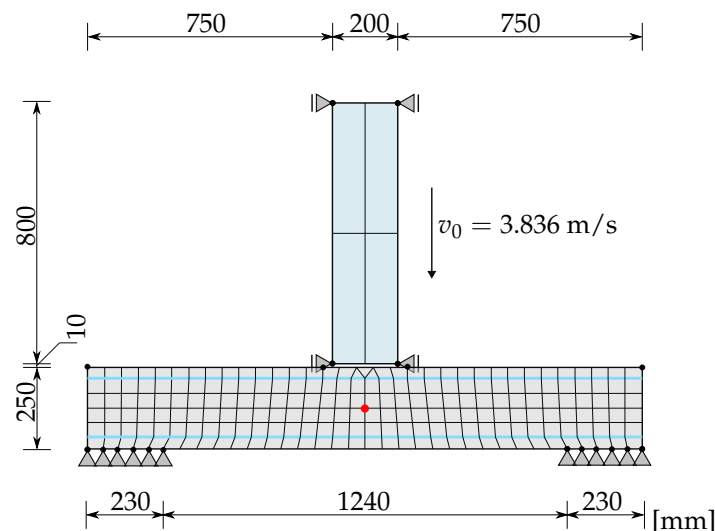


**Figure 5.** Structural scheme of a reinforced concrete member subjected to the impact of a steel punch.

The steel reinforcement bars B500B were considered an isotropic elastic material with  $E = 200$  GPa and  $\nu = 0.3$ ; for the steel S235 punch, these values were  $E = 210$  GPa and  $\nu = 0.3$ . Similarly to (1), the punch started at the simulation distance of 0.01 m from the beam, with an added initial velocity  $v_0 = 3.836$  m/s, which should correspond to a free fall from approximately 0.7 m.

When using a nonlinear explicit time integration scheme, like in this article, an adequate time step has to be chosen. The critical time step,  $\Delta t_{crit}$ , is governed by the Courant–

Friedrichs–Lewy (CFL) condition to ensure numerical stability during simulations; cf. [69]. The time step has to be smaller than the time required for a stress wave to traverse the smallest element in the mesh. The simulation time step is

$$\Delta t = \omega \Delta t_{crit} = \omega L_e \sqrt{\frac{\rho(1+\nu)(1-2\nu)}{E(1-\nu)}}$$

where  $\omega$  represents the safety factor ( $0 < \omega < 1$ , typically around 0.9),  $L_e$  the length of the smallest element, depending on its shape,  $\rho$  the density of the material,  $\nu$  the Poisson number, and  $E$  the Young modulus of elasticity. This condition, however, mainly works for simulations with linear elastic materials. In our case, since we were using nonlinear material models defined by the stress–strain curve, the final time step used was chosen to be smaller than the one calculated based on the ensured convergence of the simulations. So, for a benchmark example, the time step was  $\Delta t_{block} = 10^7$  s, and for the second model,  $\Delta t_{beam} = 10^8$  s. This time step was constant during the whole computational process.

To ensure the reliability of the numerical results and verify the independence of the solution from the spatial discretisations, a mesh sensitivity study was performed on the benchmark example. As shown in the structural scheme, see Figure 3, various mesh sizes were used (namely, 0.2 m, 0.15 m, 0.1 m, 0.05 m) for the three nonlinear material models presented in this study, plus the comparison with the linear elastic model. All the results were measured on the edge of the impacted block, and therefore in a contact zone, as represented by the red dot in Figure 3. This approach was chosen to demonstrate the time-dependent behaviour of the structures and visually comparing these behaviours, even though the results might report local indicators, rather than global structural measures. This, however, is only true for deformations. All energies presented in this article were integrated from the whole system.

For the linear elastic and viscoelastic material models, the results show fast convergence, as illustrated in Figures 6 and 7. There was almost no difference between the maximum deformations right after the impact in models with finer mesh sizes, but the coarsest mesh (0.2 m) shows great deviation compared to the others, attributable to the stiffer response inherited in the under-discretised finite element domain. The biggest difference between these two material models can, however, be seen in the behaviour of the structure after the initial impact, where, in the case of the viscoelastic model, the amplitude was visibly damped over time.

In general, the sum of kinetic, elastic, and dissipative energy must be constant and equal to the initial energy of the system, e.g., to the potential energy of gravity, given by the height of the falling body over the impact point. During the fall, the kinetic energy grows. At the time of impact, all the potential energy is converted to kinetic energy. Then, after the impact, some of the kinetic energy changes to elastic energy and to dissipative energy. At the end, when the upper body lies on the lower body, the deformation settles down. When the upper body approaches the lower one, the contact force is activated. Some local elastic deformation appears on the lower body, converted from the kinetic energy of the upper body. In the case of viscoelastic, plastic, etc., materials, a certain portion of the energy is dissipated in the form of heat or irreversible deformation. Any deformation is delayed in comparison with force, typically in the case of viscoelasticity. The largest stress corresponds to the largest deformation. Some of the deformation becomes irreversible in plastic materials.

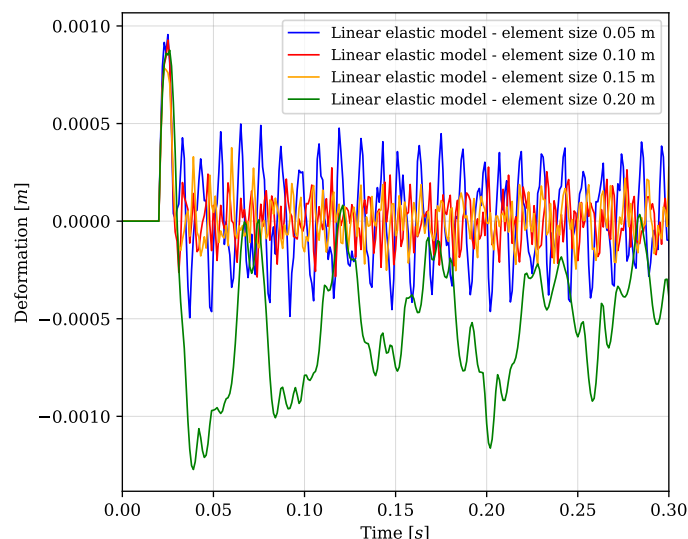


**Figure 6.** Calculated deformations in a two-block example using a linear elastic material model of concrete and different mesh sizes.

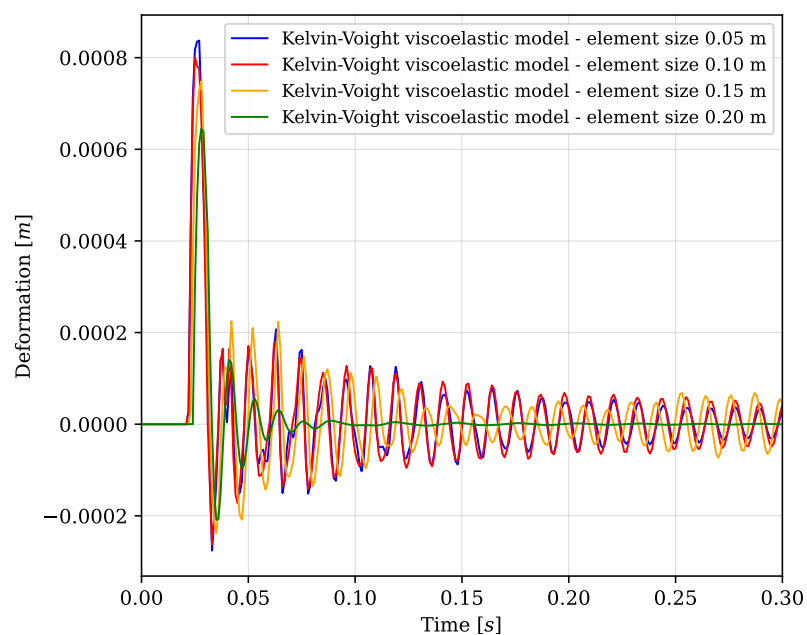


**Figure 7.** Calculated deformations in a two-block example using a Kelvin–Voight viscoelastic material model of concrete with a bilinearized diagram and different mesh sizes.

An important (critical) time corresponds to the maximal deformation of the lower body, the maximal growth of the dissipative energy, and the minimization of the kinetic energy in the system. The increase in dissipative energy is accompanied by a decrease in reflection in the upper body, i.e., a lower velocity and also a lower increase in the kinetic energy. The deformation of the lower body vanishes, except for its irreversible part. Thus, the time redistribution of deformation reflects the energy flow in the system. The rapid growth in deformation during the impact corresponds to the transfer of the kinetic energy of the falling body to the elastic energy of the contact region. Namely, a sufficiently large impact in terms of kinetic energy causes significant plastic deformation or irreversible damage, accompanied by increased influence of viscoelastic mechanisms (internal friction), manifesting as higher energy dissipation.

In the case of the Mazars damage model, the difference between the finest mesh and the coarse mesh is more significant, as shown in Figure 8, both in maximum deformation right after impact and in the time-dependent behaviour after. This can be attributed to the strain localization effect; where the finer elements are used, more damage concentrates, resulting in a softer global response. Also, the elastoplastic Rankine–Hill model exhibits critical mesh dependency, as shown in Figure 9, where a coarser mesh tends to discretise the stress concentrations over the element volume, often failing to satisfy the yield criterion in said region. Coarser models, therefore, behave more elastically, storing energy as an elastic strain rather than dissipating it through plastic work.

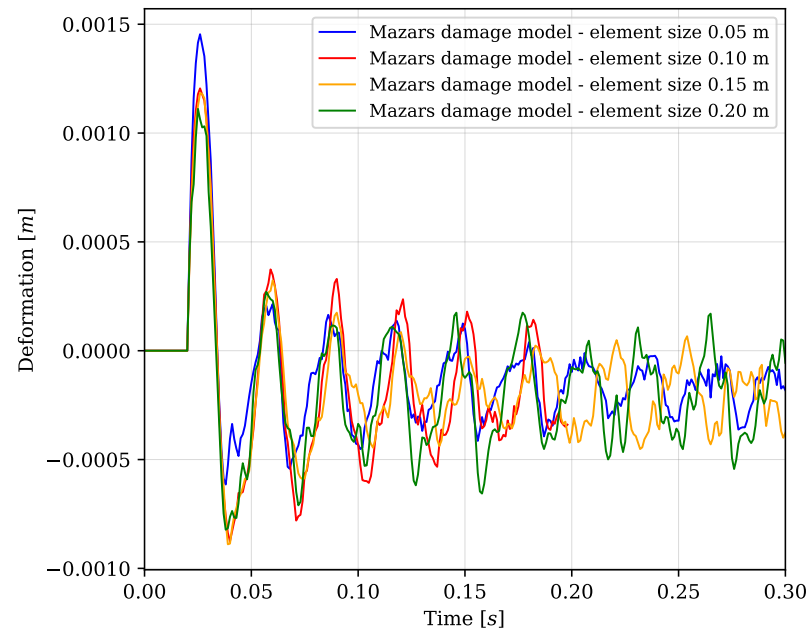


**Figure 8.** Calculated deformations in a two-block example using a damage Mazars material model of concrete with bilinearized diagram and different mesh sizes.

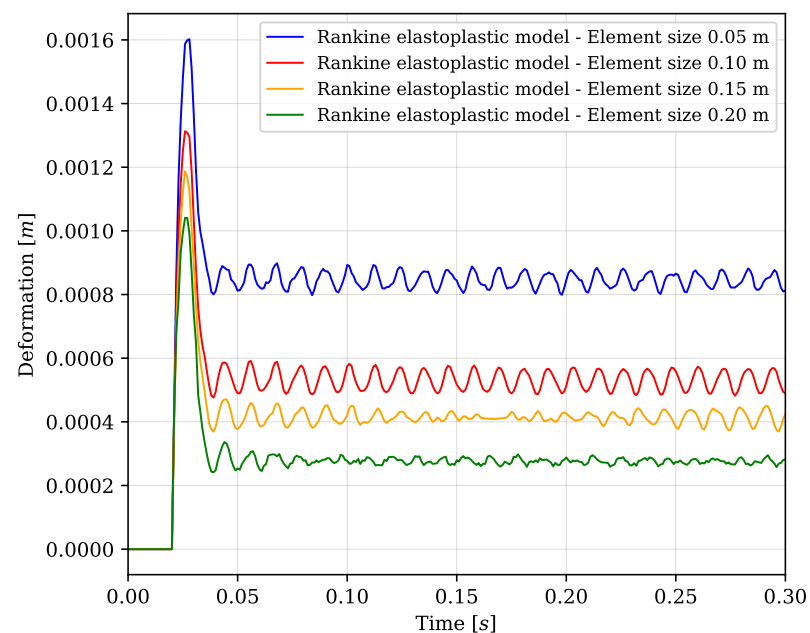


**Figure 9.** Calculated deformations in a two-block example using an elastoplastic Rankine-Hill material model of concrete with bilinearized diagram and different mesh sizes.

Throughout the impact event, the energy balance of the system was monitored to ensure the thermodynamic consistency of the numerical framework. The total energy conservation can be expressed as  $E_{tot} = E_{kin} + E_{p,int} - E_{p,ext}$ , where  $E_{tot}$  stands for the total energy of the system,  $E_{p,int}$  for potential internal energy, which is defined by its increment in every time step  $E_{p,int}^{n+1} = E_{p,int}^n + \Delta E_{p,int}$ , with  $\Delta E_{p,int} = \frac{1}{2} \Delta u^T (f_{int}^t + f_{int}^{t+\Delta t})$ , where  $\Delta u^T$  represents the displacement increment vector with internal force vectors from current and previous configurations  $f_{int}^t$  and  $f_{int}^{t+\Delta t}$ . The potential energy of external forces is handled in the same way, only with external force vectors from current and previous configurations  $f_{ext}^t$  and  $f_{ext}^{t+\Delta t}$  corresponding to the gravitational load. So, for every time step  $E_{p,ext}^{n+1} = E_{p,ext}^n + \Delta E_{p,ext}$ , where  $\Delta E_{p,ext} = \frac{1}{2} \Delta u^T (f_{ext}^t + f_{ext}^{t+\Delta t})$ . The  $\Delta u^T$  is the same displacement increment vector as presented in the above mentioned calculation of potential internal energy.

The energies for all three nonlinear material models from the benchmark example can be seen in Figures 10–12. Similar behaviour can be observed with all material models, namely a steep decline in kinetic energy (red) right after the impact with a partial increase after. Because the kinetic energy is calculated for the whole system, this rise is caused by the impacting block bouncing back up. Also, since the potential internal energy was calculated from the displacement increment vector and internal force vectors, it combined both elastic and nonelastic (dissipative) energy  $E_{p,int} = E_{el} + E_{diss}$ . Therefore, dissipative energy cannot, in this case, be higher than  $E_{p,int}$ , and of course, it also cannot surpass the initial kinetic energy value. These rules serve as good indicators of the correctness of the results.

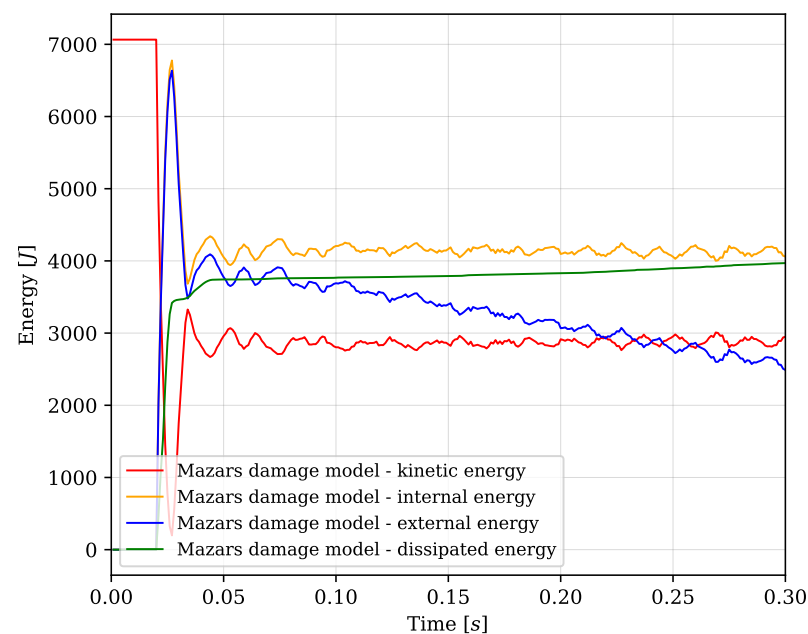


**Figure 10.** Calculated energies using Mazars damage model with bilinearized diagram of concrete from benchmark two-block example.

A direct comparison of the dissipated energies extracted from the benchmark example is shown in Figure 13. For better evaluation, the dissipated energies were normalized by the system's initial kinetic energy ( $E_{diss}/E_{kin}^0$ ). This normalization strategy demonstrates the impact energy absorption efficiency, eliminating the dependence on absolute energy magnitudes and allowing for a meaningful comparison across the disparate dissipation mechanisms of all three used material models. From the shapes of the curves, it can be seen that the viscoelastic material model dissipates energy less steeply than the damage and elastoplastic ones, which rise almost immediately after the impact. When comparing damage and elastoplastic material models, the percentage difference in their highest defor-

mations is roughly 9.38%, (1.45 mm Mazars, 1.6 mm Rankine–Hill), but the Rankine–Hill elastoplastic model shows 53% more effectiveness in dissipating energy.

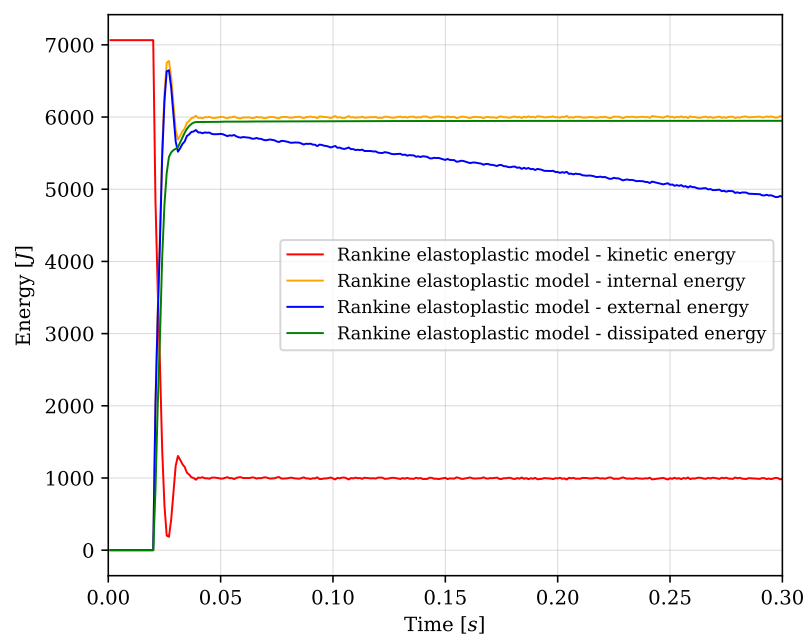


**Figure 11.** Calculated energies using elastoplastic Rankine–Hill material model with bilinearized diagram of concrete from benchmark two-block example.

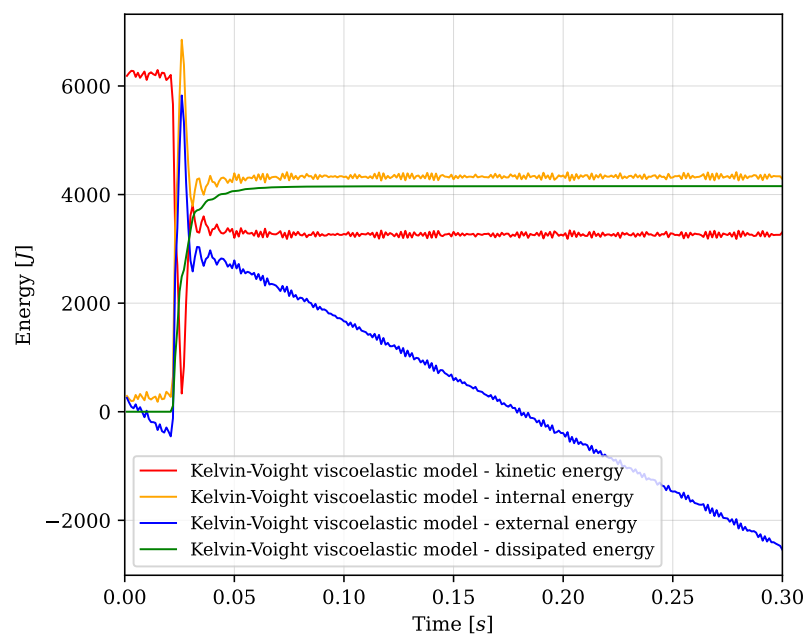


**Figure 12.** Calculated energies using viscoelastic Kelvin–Voigt material model with bilinearized diagram of concrete from the benchmark two-block example.

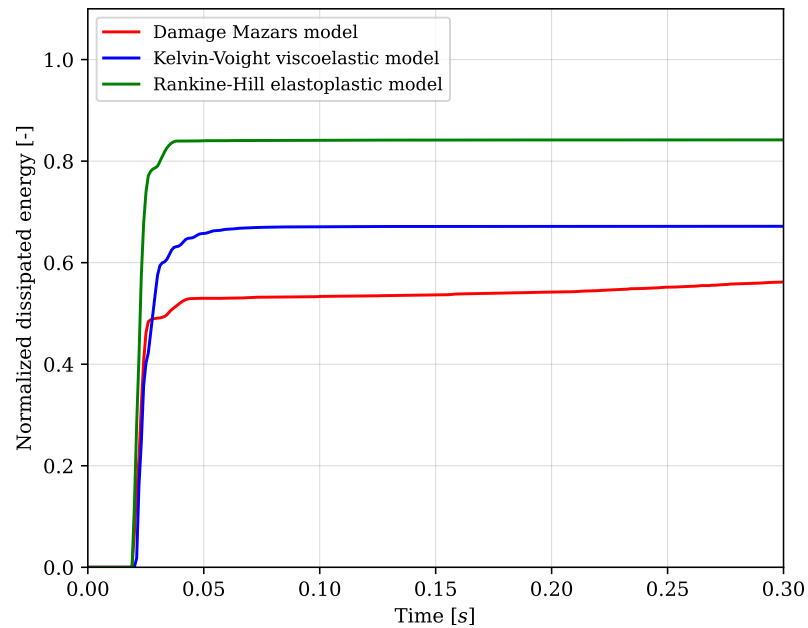


**Figure 13.** Normalized dissipative energies by the initial kinetic energy of the system from the benchmark example.

An explanation of this phenomenon is shown in Figure 14, demonstrating the constitutive laws of the elastoplastic and damage model, where the volume of the dissipated energy clearly favors the second one. With the viscoelastic model, the volume depends on the choice of parameter  $\beta$ . These were the prime sources of energy dissipation measured; however, as with all nonlinear calculations, a small amount might be lost during the numerical iterations. These can be minimised by choosing a small enough time step and corresponding mesh size.

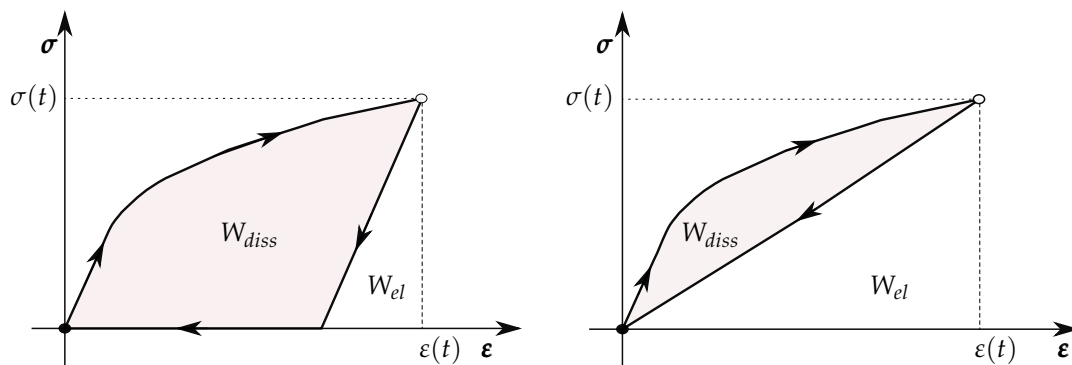


**Figure 14.** Difference in the volume of dissipated energy when considering elastoplastic (left) and damage (right) material models, where  $W_{diss}$  represents the dissipated energy and  $W_{el}$  the elastic one.

The second example represents a more realistic case of a reinforced concrete beam under the impact of a steel punch. Reinforcement was modelled using beam finite elements and a linear elastic material model because of the usage of a stress–strain diagram with a softening part to simulate concrete behaviour. Deformations were measured in a node represented by a red dot (see Figure 5). The results are compared in Figure 15. There is a significant difference between the deformations of the beam when using the damage Mazars model compared to other models. The reason for this is that the concrete undergoes a great stiffness degradation caused by the small tensile strength, causing the material to become more compliant and deform further under the same inertial load.

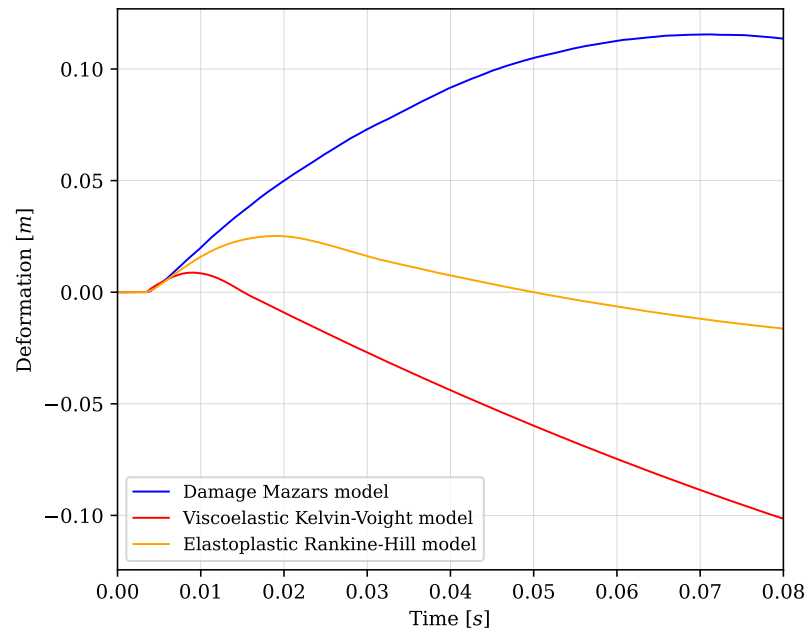


**Figure 15.** Deformations of the concrete beam impacted by a steel punch for all three material models.

On the other hand, thanks to the nonlinear supports used in this simulation, both viscoelastic and elastoplastic models suffer from negative deformations after the initial impact. This is caused by the inertial force due to the parts of the beam that remained elastic. This explains why this phenomenon is more visible with the viscoelastic model, where there is no plasticity or damage present to dissipate the initial impact energy. All dissipated energies from the second example were again normalized by the initial kinetic energy, as presented in Figure 16. Here, it seems that all three material models have a similar dissipated energy ratio to each other. However, when taking into account the deformations, the damage Mazars model again stands out, with a 4.8 times higher maximum deformation than the Rankine–Hill elastoplastic model while sharing almost the same dissipation ratio around 65%.

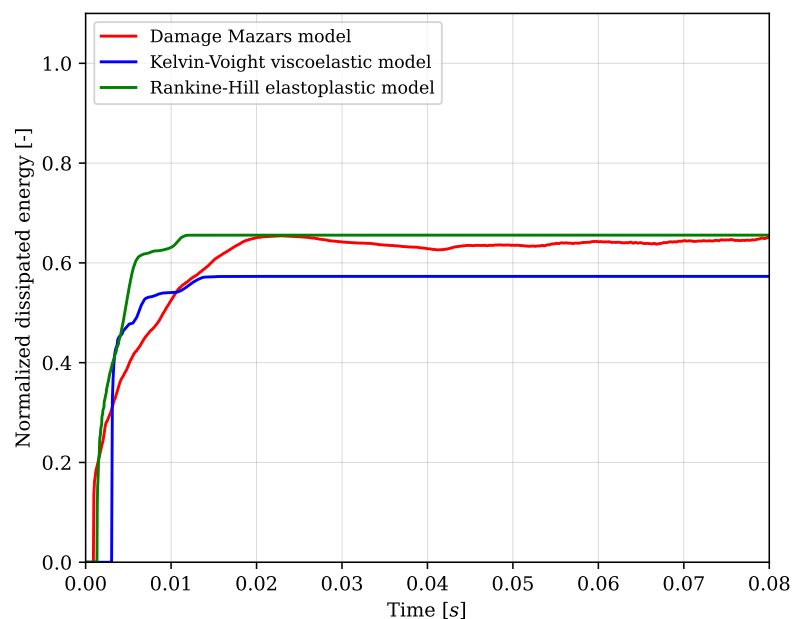


**Figure 16.** Normalized dissipative energies by the initial kinetic energy of the system from the concrete beam and steel punch simulation for all three material models.

Finally, the calculated energies in the system for all nonlinear material models (see Figures 17–19) are presented; the bigger measured distance between internal potential energy and dissipated energy when compared to the first example is clearly visible. The reason for this is that the linear elastic rebar provides a mechanism for storing elastic strain energy even after the concrete degrades or yields. The biggest difference can be seen when using the Mazars damage model, where the concrete is apparently unable to sustain the load, and the structural integrity is held by the rebar.

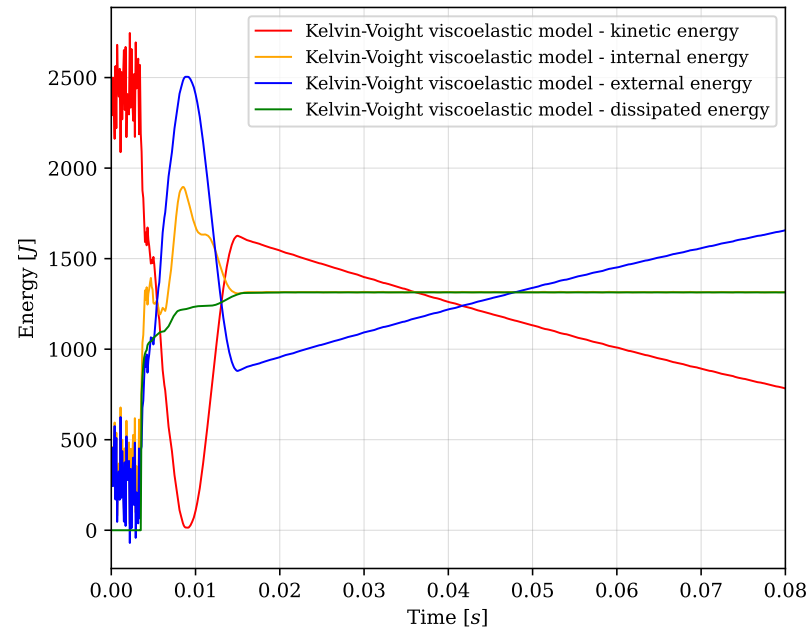


**Figure 17.** Calculated energies of the concrete beam impacted by a steel punch using a viscoelastic Kelvin–Voigt model simulating concrete.

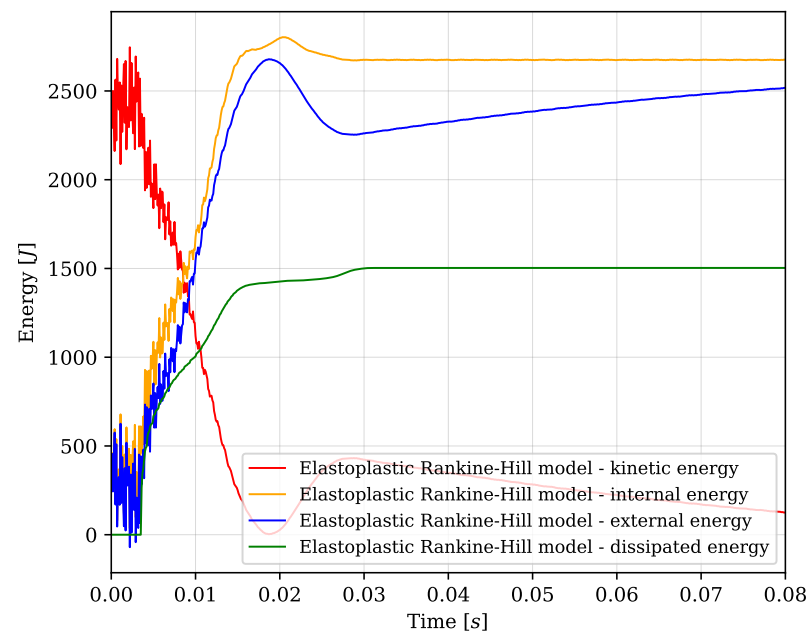


**Figure 18.** Calculated energies of the concrete beam impacted by a steel punch using an elastoplastic Rankine–Hill material model with a realistic stress–strain curve simulating concrete.

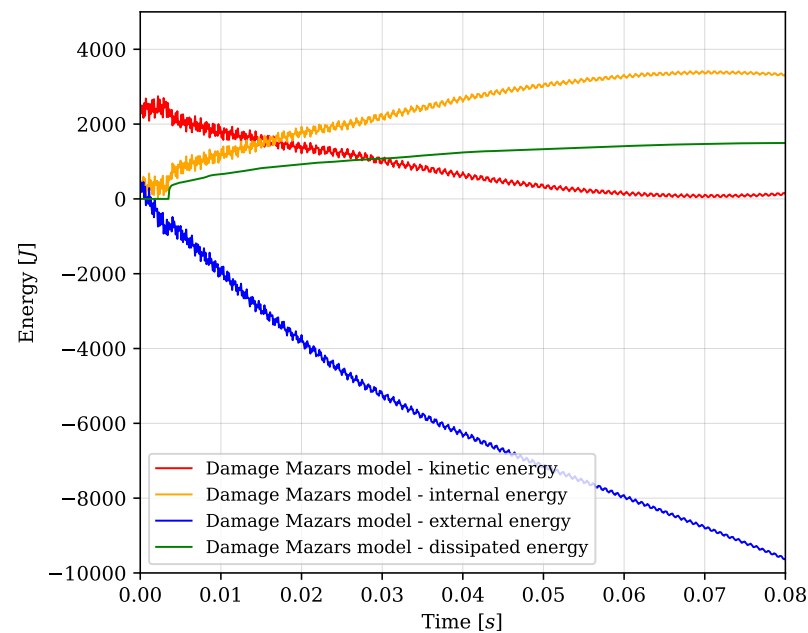


**Figure 19.** Calculated energies of the concrete beam impacted by a steel punch using Mazars damage material model with a realistic stress–strain curve simulating concrete.

## 5. Conclusions

Two computational contact/impact simulations were performed in this study, applying three different material models: (a) the Kelvin–Voigt viscoelastic model, (b) the elastoplastic model applying the Rankine–Hill criterion, and (c) the Mazars damage model. The purpose was to analyse and compare their responses in terms of deformation and dissipated energy under dynamic loading scenarios. The first simulation involved the vertical impact of two blocks (steel on concrete one), while the second one featured a practical case of a reinforced concrete beam subjected to the free fall of a steel punch. In both cases, the simulations were carried out using a commercial FEM solver with explicit time integration and shell elements representing structural components. The contact interactions were modelled using line-to-line contact. The results clearly demonstrate that each material model produces distinct mechanical responses. The Mazars damage model consistently exhibited the lowest deformation-to-energy dissipation ratio due to its strict damage criteria, which caused damage to propagate rapidly through the structure and led to severe stiffness degradation, as presented in the second example. In contrast, the elastoplastic model exhibited higher dissipation, with localised plastic deformation due to the less strict criteria. The Kelvin–Voigt model where energy dissipation occurred solely due to viscous damping was also used for comparison.

Ultimately, the study illustrates that material model selection significantly influences the simulation results. While the Rankine–Hill and Kelvin–Voigt models may yield similar dissipated energy in some scenarios, this similarity is highly dependent on the chosen viscosity parameter in the second model. Such partial results, induced by Section 4, are evidently not the final aims of the research. The results presented in Figure 15 do not agree with the available experimental ones; cf. [66]. Nevertheless, they can be interpreted in such a way that a realistic model of material and structural behaviour can be compounded from appropriate elastic, viscous, plastic, and damage models. Such a model is under development now. Additional research challenges derive from the appropriate formulation of (frequently ill-posed) inverse problems of the design of material characteristics and identification of their parameters and their computational analysis; for partial approaches and results, cf. [70,71]. The assertion of some further physical processes may be important,

too, for the deeper analysis of energy dissipation on (potential) contacts  $\Lambda$ . The authors' team considers this a research priority for the near future.

**Author Contributions:** Conceptualization and methodology, I.N. and J.V.; numerical methods and computational algorithms, M.T.; software development, O.H., M.K. and T.D. All authors have read and agreed to the published version of the manuscript.

**Funding:** This study has been supported by the project of specific university research at Brno University of Technology No. FAST-S-25-8850.

**Data Availability Statement:** The data presented in this study are available on request from the corresponding author.

**Conflicts of Interest:** Author Ivan Němec is employed by the FEM Consulting Ltd. The remaining authors declare that the research was conducted in the absence of any commercial or financial relationships that could be construed as a potential conflict of interest.

## References

- Bermúdez de Castro, A. *Continuum Thermomechanics*; Birkhäuser: Basel, Switzerland, 2005.
- Papenfuß, C. *Continuum Thermodynamics and Constitutive Theory*; Springer: Berlin/Heidelberg, Germany, 2020.
- Trcala, M.; Suchomelová, P.; Bošanský, M.; Hokeš, F.; Němec, I. The generalized Kelvin chain-based model for an orthotropic viscoelastic material. *Mech. Time-Depend. Mater.* **2024**, *28*, 1639–1659. [[CrossRef](#)]
- Wang, Y.; Pan, Z.; Zeng, B.; Xu, Q. Cyclic creep model of concrete based on Kelvin chain under fatigue loads. *Constr. Build. Mater.* **2024**, *417*, 135255. [[CrossRef](#)]
- Al Janaideh, M.; Krejčí, P.; Monteiro, G.A. Memory reduction of rate-dependent Prandtl–Ishlinskii compensators in applications on high-precision motion systems. *Physica B* **2024**, *677*, 415595.
- Lourenco, P.B.; de Borst, R.; Rots, J.G. A plane stress softening plasticity model for orthotropic materials. *Int. J. Numer. Methods Eng.* **1997**, *40*, 4033–4057. [[CrossRef](#)]
- van den Heever, M.; Bester, F.; Kruger, J.; van Zijl, G. Numerical modelling strategies for reinforced 3D concrete printed elements. *Addit. Manuf.* **2022**, *50*, 102569. [[CrossRef](#)]
- Minh, H.-L.; Khatir, S.; Wahab, M.A.; Cuong-Le, T. A concrete damage plasticity model for predicting the effects of compressive high-strength concrete under static and dynamic loads. *J. Build. Eng.* **2021**, *44*, 103239. [[CrossRef](#)]
- Hashiguchi, K. *Elastoplasticity Theory*; Springer: Tokyo, Japan, 2014.
- Welander, A.; Kinnunen, I.; Daneryd, A.; Hajek, J.; Sahu, K.; Mousavi, M. Tailored energy dissipation with viscoelastic architected materials. *Mech. Mater.* **2025**, *201*, 105216. [[CrossRef](#)]
- Gouhier, F.; Diani, J. A comparison of finite strain viscoelastic models based on the multiplicative decomposition. *Eur. J. Mech. A/Solids* **2024**, *108*, 105424. [[CrossRef](#)]
- Vavourakis, V.; Loukidis, D.; Charnpis, D.C.; Papanastasiou, P. Assessment of remeshing and remapping strategies for large deformation elastoplastic finite element analysis. *Comput. Struct.* **2013**, *114–115*, 133–146. [[CrossRef](#)]
- Léger, S.; Pepin, A. An updated Lagrangian method with error estimation and adaptive remeshing for very large deformation elasticity problems: The three-dimensional case. *Comput. Methods Appl. Mech. Eng.* **2016**, *309*, 1–18. [[CrossRef](#)]
- Anantheswar, A.; Wollny, I.; Kaliske, M. Treatment of inelastic material models within a dynamic ALE formulation for structures subjected to moving loads. *Int. J. Numer. Methods Eng.* **2025**, *126*, e7599. [[CrossRef](#)]
- Li, B.; Li, P.; Zhou, R. Feng, X.-Q., Zhou, K. Contact mechanics in tribological and contact damage-related problems: A review. *Tribol. Int.* **2022**, *171*, 107534. [[CrossRef](#)]
- Zhang, J.; Liang, X.; Zhang, Z.; Feng, G.; Zhao, Q.; Zhao, L.; He, G. A continuous contact force model for impact analysis. *Mech. Syst. Signal Process.* **2022**, *168*, 108739. [[CrossRef](#)]
- Zheng, M.; Tong, M.; Li, Y.; Pan, X.; Dong, Q. A new compliant contact force model for impact analysis. *Multibody Sys. Dyn.* **2026**, *66*. [[CrossRef](#)]
- Pham, T.P.; Chen, W.; Hao, H. Review on impact response of reinforced concrete beams: Contemporary understanding and unsolved problems. *Adv. Struct. Eng.* **2021**, *24*, 2282–2303. [[CrossRef](#)]
- Jin, L.; Zhang, X.; Zhang, R.; Du, X. Effect of impact location on the dynamic response of concrete columns reinforced with GFRP bars having various slenderness ratios: A numerical study. *Structures* **2024**, *69*, 107571. [[CrossRef](#)]
- Kang, S.-H.; Lee, S.-M.; Shin, S.J. Improved area regularization technique for penalty-method-based node-to-segment contact analysis. *Comput. Mech.* **2023**, *71*, 801–825. [[CrossRef](#)]

21. Jin, S.; Sohn, D.; Im, S. Node-to-node scheme for three-dimensional contact mechanics using polyhedral type variable-node elements *Comput. Methods Appl. Mech. Eng.* **2016**, *304*, 217–242. [[CrossRef](#)]
22. Batistić, I.; Cardiff, P.; Tuković, Ž. A finite volume penalty based segment-to-segment method for frictional contact problems. *Appl. Math. Modell.* **2022**, *101*, 673–693. [[CrossRef](#)]
23. González, J.A.; Kopačka, J.; Kolman, R.; Park, K.-C. Partitioned formulation of contact-impact problems with stabilized contact constraints and reciprocal mass matrices. *Int. J. Numer. Methods Eng.* **2021**, *122*, 4609–4636. [[CrossRef](#)]
24. Němec, I.; Vala, J.; Štekbauer, H.; Jedlička, M.; Burkart, D. New methods in collision of bodies analysis. In Proceedings of the 21st Programs and Algorithms of Numerical Mathematics (PANM), Jablonec nad Nisou, Czech Republic, 19–24 June 2022; Institute of Mathematics CAS: Prague, Czech Republic, 2023; pp. 133–148.
25. Xiang, D.; Shen, Y.; Wei, Y.; You, M. A comparative study of the dissipative contact force models for collision under external spring forces. *J. Comput. Nonlinear Dynam.* **2018**, *13*, 101009. [[CrossRef](#)]
26. Wang, G.; Liu, C.; Liu, Y. Energy dissipation analysis for elastoplastic contact and dynamic dashpot models. *Int. J. Mech. Sci.* **2022**, *221*, 107214. [[CrossRef](#)]
27. Wang, G.; Jia, W.; Cheng, F.; Flores, P. An enhanced contact force model with accurate evaluation of the energy dissipation during contact-impact events in dynamical systems. *Appl. Math. Modell.* **2024**, *135*, 51–72. [[CrossRef](#)]
28. Huang, H.; Yao, Y.; Liang, C.; Ye, Y. Experimental study on cyclic performance of steel-hollow core partially encased composite spliced frame beam. *Soil Dyn. Earthq. Eng.* **2022**, *163*, 107499. [[CrossRef](#)]
29. Wang, M.; Xu, X.; Yue, Q.; Wang, Y. A comprehensive survey and experimental comparison of graph-based approximate nearest neighbor search. In Proceedings of the 47th Very Large Data Bases (VLDB), Copenhagen, Denmark, 16–20 August 2021; VLDB Endowment: Stanford, CA, USA, 2021; pp. 1964–1978.
30. Vala, J.; Rek, V. On a computational approach to multiple contacts/impacts of elastic bodies. In Proceedings of the 22th Programs and Algorithms of Numerical Mathematics (PANM), Jablonec nad Nisou, Czech Republic, 19–24 June 2022; Institute of Mathematics CAS: Prague, Czech Republic, 2023; pp. 269–280.
31. Ouyang, Q.; Zhuang, X.; Rabczuk, T.; Ning, Y.; Kang, G.; Chen, P. Implementation of three-dimensional contact algorithm in numerical manifold method for the structural impact simulation. *Int. J. Impact Eng.* **2024**, *193*, 105040. [[CrossRef](#)]
32. Huang, H.; Yao, Y.; Zhang, W.; Zhou, L. A push-out test on partially encased composite column with different positions of shear studs. *Eng. Struct.* **2023**, *289*, 116343. [[CrossRef](#)]
33. Assie, A.E.; Eltaher, M.A.; Mahmoud, F.F. Modeling of viscoelastic contact-impact problems. *Appl. Math. Modell.* **2010**, *34*, 2336–2352. [[CrossRef](#)]
34. Fernández, J.R.; Santamarina, D. A dynamic viscoelastic contact problem with normal compliance. *J. Comput. Appl. Math.* **2015**, *276*, 30–46. [[CrossRef](#)]
35. Wang, D.; de Boer, G.; Neville, A.; Ghanbarzadeh, A. A review on modelling of viscoelastic contact problems. *Lubricants* **2022**, *10*, 358. [[CrossRef](#)]
36. Mandriota, C.; Menga, N.; Carbone, G. Enhancement of adhesion strength in viscoelastic unsteady contacts. *J. Mech. Phys. Solids* **2024**, *192*, 105826. [[CrossRef](#)]
37. Piska, R.; Sivadas, K.; Boyina, K.; Vuppuluri, A.; Chaur, A. Recent trends in computational damage models: An overview. *Theor. Appl. Fract. Mech.* **2024**, *132*, 104494. [[CrossRef](#)]
38. Edalat Behbahani, A.; Barros, J.A.O.; Ventura-Gouveia, A. Plastic-damage smeared crack model to simulate the behaviour of structures made by cement based materials. *Int. J. Solids Struct.* **2015**, *73–74*, 20–40. [[CrossRef](#)]
39. Qasem, M.; Hasan, M.; Muhamad, R.; Chin, C.-L.; Alanazi, N. Generalised calibration and optimization of concrete damage plasticity model for finite element simulation of cracked reinforced concrete structures. *Results Eng.* **2025**, *25*, 103905. [[CrossRef](#)]
40. Mazars, J. A description of micro- and macroscale damage of concrete structure. *Eng. Fract. Mech.* **1986**, *25*, 729–737. [[CrossRef](#)]
41. Mazars, J.; Hamon, F.; Grange, S. A new 3D damage model for concrete under monotonic, cyclic and dynamic loadings. *Mater. Struct.* **2015**, *48*, 3779–3793. [[CrossRef](#)]
42. Arruda, M.R.T.; Pacheco, J.; Castro, L.M.S.; Julio, E. A modified Mazars damage model with energy regularization. *Eng. Fract. Mech.* **2022**, *259*, 108129. [[CrossRef](#)]
43. Debuisne, M.; Davenne, L.; Jason, L. On the need of compressive regularization in damage models for concrete: Demonstration on a modified Mazars model. *Appl. Mech.* **2024**, *5*, 490–512. [[CrossRef](#)]
44. Desmorat, R. Anisotropic damage modeling of concrete materials. *Int. J. Damage Mech.* **2016**, *25*, 818–852. [[CrossRef](#)]
45. Jahanitabar, A.A.; Lotfi, V. Formulation and efficient implementation of coupled anisotropic damage-plasticity model for plain concrete. *Acta Mech.* **2024**, *235*, 4575–4605. [[CrossRef](#)]
46. Wang, L.-X.; Wen, L.-F.; Tian, R.; Feng, C. Improved XFEM (IXFEM): Arbitrary multiple crack initiation, propagation and interaction analysis. *Comput. Methods Appl. Mech. Eng.* **2024**, *421*, 116791. [[CrossRef](#)]
47. Gong, W.; Li, H.; Zhang, Q. Improved enrichments and numerical integrations in SGFEM for interface problems. *J. Comput. Appl. Math.* **2024**, *438*, 115540. [[CrossRef](#)]

48. González-Albuixech, V.; Giner, E.; Gravouil, A. Analysis of stress intensity factor oscillations in 3D cracks using domain integrals and the extended finite element method. *Comput. Methods Appl. Mech. Eng.* **2025**, *436*, 117739. [[CrossRef](#)]
49. Kozák, V.; Vala, J. Some peculiarities of using the extended finite element method in modelling the damage behaviour of fibre-reinforced composites. *Materials* **2025**, *18*, 1787. [[CrossRef](#)]
50. Vala, J.; Tomáš, J. Damage behaviour of quasi-brittle composites: Mathematical and computational aspects. *Appl. Sci.* **2025**, *15*, 4214. [[CrossRef](#)]
51. Tran, H.T.; Bui, T.Q. A nonlocal gradient damage model with energy limiter for dynamic brittle fracture. *Comput. Mech.* **2024**, *73*, 831–856. [[CrossRef](#)]
52. Lv, W.; Lu, G.; Xia, X.; Gu, X.; Zhang, Q. Energy degradation mode in nonlocal Macro-Meso-Scale damage consistent model for quasi-brittle materials. *Theor. Appl. Fract. Mech.* **2024**, *130*, 104288. [[CrossRef](#)]
53. Vilppo, J.; Kouhia, R.; Hartikainen, J.; Kolari, K.; Fedoroff, A.; Calonius, K. Anisotropic damage model for concrete and other quasi-brittle materials. *Int. J. Solids Struct.* **2021**, *225*, 111048. [[CrossRef](#)]
54. Kružík, M.; Roubíček, T. *Mathematical Methods in Continuum Mechanics of Solids*; Springer: Cham, Switzerland, 2019.
55. Krömer, S.; Kružík, M.; Morandotti, M.; Zappale, E. Measure-valued structured deformations. *J. Nonlin. Sci.* **2024**, *34*, 100. [[CrossRef](#)]
56. Pommaret, J.F. Parametrization of Cosserat equations. *Acta Mech.* **2010**, *215*, 43–55. [[CrossRef](#)]
57. Németh, B.; Adhikari, R. A geometric formulation of Schaefer’s theory of Cosserat solids. *J. Math. Phys.* **2024**, *65*, 061902. [[CrossRef](#)]
58. Tomáš, J.; Petrák, F. Higher-order and Weil Grassmannian as a space of subalgebras of a Weil algebra. *Filomat* **2024**, *38*, 7755–7773. [[CrossRef](#)]
59. Barták, J.; Herrmann, L.; Lovicar, V.; Vejvoda, O. *Partial Differential Equations of Evolution*; Ellis Horwood: London, UK, 1991.
60. Roubíček, T. *Nonlinear Partial Differential Equations with Applications*; Birkhäuser: Basel, Switzerland, 2005.
61. Drábek, P.; Milota, I. *Methods of Nonlinear Analysis*; Birkhäuser: Basel, Switzerland, 2013.
62. Vala, J. Numerical approaches to the modelling of quasi-brittle crack propagation. *Arch. Math.* **2023**, *59*, 295–303. [[CrossRef](#)]
63. Rektorys, K. *Variational Methods in Mathematics, Science and Engineering*; D. Reidel: Dordrecht, The Netherlands, 1977.
64. Rektorys, K. *The Method of Discretization in Time and Partial Differential Equations*; D. Reidel: Dordrecht, The Netherlands, 1982.
65. Brézis, H. Équations et inéquations non-linéaires dans les espaces vectoriel en dualité. *Ann. Inst. Fourier* **1968**, *18*, 115–176. [[CrossRef](#)]
66. Trcala, M.; Němec, I.; Vaněčková, A.; Hokeš, F. Dynamic analysis of viscous material models. In Proceedings of the 20th Programs and Algorithms of Numerical Mathematics (PANM), Hejnice, Czech Republic, 21–26 June 2020; Institute of Mathematics CAS: Prague, Czech Republic, 2021; pp. 139–148.
67. Yang, Y.; Lin, B.; Zhang, W. Experimental and numerical investigation of an arch–beam joint for an arch bridge. *Arch. Civ. Mech. Eng.* **2023**, *23*, 101. [[CrossRef](#)]
68. Bourdin, L.; Caubet, F.; de Cordemoy, A.J. Sensitivity analysis of a scalar mechanical contact problem with perturbation of the Tresca’s friction law. *J. Optim. Theory Appl.* **2022**, *192*, 856–890. [[CrossRef](#)]
69. Gnedin, N.Y.; Semenov, V.A.; Kravtsov, A.V. Enforcing the Courant–Friedrichs–Lewy condition in explicitly conservative local time stepping schemes. *J. Comput. Phys.* **2018**, *359*, 93–105. [[CrossRef](#)]
70. Song, J.; Gu, R.J. A finite element-based methodology for inverse problem of determining contact forces using measured displacements. *Inverse Probl. Sci. Eng.* **2012**, *20*, 769–783. [[CrossRef](#)]
71. Sahin, T.; von Danwitz, M.; Popp, A. Solving forward and inverse problems of contact mechanics using physics-informed neural networks. *Adv. Model. Simul. Eng. Sci.* **2024**, *11*, 11. [[CrossRef](#)]

**Disclaimer/Publisher’s Note:** The statements, opinions and data contained in all publications are solely those of the individual author(s) and contributor(s) and not of MDPI and/or the editor(s). MDPI and/or the editor(s) disclaim responsibility for any injury to people or property resulting from any ideas, methods, instructions or products referred to in the content.